

THESIS FOR THE DEGREE OF LICENTIATE OF ENGINEERING

**Design of a fault-tolerant fractional slot PMSM
for a vehicle application**

CHRISTIAN DU-BAR



Division of Electric Power Engineering
Department of Energy and Environment
CHALMERS UNIVERSITY OF TECHNOLOGY
Göteborg, Sweden 2015

**Design of a fault-tolerant fractional slot PMSM
for a vehicle application**

Christian Du-Bar

© Christian Du-Bar, 2015.
except where otherwise stated.
All rights reserved

Department of Energy and Environment
CHALMERS UNIVERSITY OF TECHNOLOGY
SE-412 96 Göteborg
Sweden
Telephone + 46 (0)31 772 00 00

Abstract

In automotive applications, the PMSM is an interesting alternative due to the high efficiency requirement; as only a limited amount of energy can be stored in the relatively expensive battery. Another advantage is the high torque and power density since it is very important to save especially space but also weight in vehicle applications. As the battery technology develops, pure electric cars are expected to become a more and more interesting alternative. In case of pure electric vehicles, it is natural that the requirement of reliability on the electric drive system becomes an aspect of utmost importance as the electric drive is the only driving force.

In this thesis a three phase fractional slot PMSM is designed and its possibility to operate and to deliver an acceptable quality of performance even after a fault occurs is investigated. The faults investigated are phase open circuit and phase short circuit, and it is shown that the thesis machine design can be operated during both circumstances. During normal operation, the fault-tolerant machine design shows a similar performance as an existing design of the same size, where fault-tolerance was not considered in the design. During fault, the maximum torque is reduced by approximately 50 % and the maximum speed is reduced to roughly 1/3 or 1/4 of the maximum speed in case of a phase open circuit fault or a phase short circuit fault respectively. A semi-analytical machine modeling approach are used to model the individual saturation levels of the phases successfully. The same model is used to calculate new current waveforms that are used to reduce the torque ripple during the unbalanced conditions associated with the operation during fault. Further, a design procedure considering the machine design performance in relation to its expected material cost is used and presented.

Keywords

Permanent magnet synchronous machine (PMSM), Fractional slot, Concentrated windings, Fault-tolerance, Unbalanced operation, Saturation, Efficiency.

Acknowledgements

The financial support from the Swedish innovation agency Vinnova via the former xEVCO project including Volvo Cars and SP, which this PhD project was a part of, is gratefully appreciated.

I would like to thank my main supervisor and examiner Torbjörn Thiringer for his great support and always very quick response with input and feedback. I would of course also like to address special thanks to my supervisors Sonja Lundmark and Mikael Alatalo for their support and valuable input and comments. Through all three of you in a combination, I think the quality of my work really has been increased an extra level or two.

I would also like to thank all my colleagues, room-mates and friends at the Division of Electric Power Engineering for creating such a nice and fun environment to work in. Thanks also to the people one stair down at the Division of High Voltage Engineering, they also contribute to the appreciated working environment.

Finally, I would like to thank my family including my wonderful fiancée Gabriela for endless love and support over the years.

Christian Du-Bar
Göteborg, November 2014

Contents

Abstract	iii
Acknowledgements	v
Introduction	1
1 Machine Design Modeling	5
1.1 Electric and magnetic loading	5
1.2 Permanent magnet flux	7
1.3 Core loss and core geometry	8
1.4 Thermal conductivity of the winding mix	10
1.5 Pole and slot combinations	12
1.6 Winding factor	13
1.7 MMF time and space harmonics	15
1.8 Inductance calculation	19
2 Dynamic Modeling of PMSMs	23
2.1 Basic 3ph-model	23
2.2 Flux model in the rotating dq-reference frame	25
2.3 Basic modeling of chosen faults	26
2.3.1 Phase short circuit	27
2.3.2 Phase open circuit	27
2.4 Control	29
2.4.1 Ordinary PI controller	29
2.4.2 Resonant and PI controller	29
2.5 Converter limitations	30
3 Design of fault-tolerant fractional slot machines	35
3.1 Design specification	35
3.1.1 Rating of the reference machine	36
3.2 Selection of pole and slot combination	38
3.3 FEA and material data	43

3.3.1	Finite Element Analysis	43
3.3.2	Material data	43
3.4	Design strategy	44
3.4.1	Design variables	44
3.4.2	Design variable combinations	46
3.4.3	From design variables to geometry parameters	46
4	Analysis of fault-tolerant fractional slot machine designs	49
4.1	Machine design selection	49
4.1.1	Estimation of the current material costs	49
4.1.2	Torque per cost for different cost scenarios	51
4.1.3	Cost efficiency of the 12/5 machine designs	53
4.1.4	Cost efficiency of the 24/11 machine designs	57
4.1.5	Torque speed characteristics of the 12/5 machine designs	61
4.1.6	Torque speed characteristics of the 24/11 machine designs	62
4.2	The two selected machine designs	63
4.2.1	Estimation of end-windings	63
4.2.2	Turn selection	65
4.2.3	Thermal impact of the slot geometry	66
4.2.4	Thermal restriction of the electric loading	68
4.3	Efficiency	70
4.4	Summary of comparison	74
5	Per phase flux machine model	75
5.1	Flux representation in a single phase	75
5.1.1	Per phase flux and torque maps	77
5.2	Numerical solution of 2-phase MTPA operation	81
6	Further analysis of one fault-tolerant fractional slot machine design	83
6.1	Unbalanced operation using resonant controller	84
6.1.1	Phase open circuit	84
6.1.2	Phase short circuit	89
6.2	Numerically calculated unbalanced operating points	92
6.2.1	Filtering of numerically calculated currents	92
6.2.2	Torque speed characteristics	93
6.2.3	Efficiency	95
6.3	2D modeling of MMF harmonic content and losses on the rotor side	97
7	Conclusions and future work	101
7.1	Conclusions	101
7.2	Future Work	103

Introduction

Background

Permanent magnet synchronous machines (PMSM) of different sizes are used in a great number of applications. They are often competitive in the low power region due to high efficiency, and in the medium power region due to high torque and power density. At higher power levels, PMSM are sometimes used as wind power generators, also offering the possibility to remove the gear box and operate in a direct-drive configuration. The PMSM are often categorized depending on the permanent magnet (PM) and rotor configuration as well as the flux path and air-gap arrangement. The PM can be surface-mounted or interior-mounted and the same stator can be used for both types of machines. Further, the PMSM can be divided into radial flux machines where the magnetic flux is crossing the air-gap in the radial direction and axial flux machines where the magnetic flux crosses the air-gap in the axial direction. Again, it is often possible to utilize the same pole, slot and winding configuration. A third group is the transverse flux machines, that benefit from the involvement of a more complicated magnetic circuit in favor of a simpler electrical circuit.

In automotive applications, the PMSM is an interesting alternative due to the high efficiency requirement; as only a limited amount of energy can be stored in the relatively expensive battery. Another advantage is the high torque and power density since it is very important to save especially space but also weight in vehicle applications. The introduction of electric drives into vehicles may improve the fuel economy and reduce the environmental emissions but allows also for new features such as increased safety and passenger comfort. As the battery technology develops, pure electric cars are expected to become a more and more interesting alternative. In case of pure electric vehicles, it is natural that the requirement of reliability on the electric drive system becomes a more important aspect as the electric drive is the only driving force. According to [1], the trend towards autonomic control systems increases the interest of fault-tolerant capability in automotive applications. It is therefore of interest to combine the advantages of high efficiency, torque and power density associated

with PMSM and the ability of operation during isolated failures in the machine or the converter. In [2], it is stated that the introduction of fault-tolerance into the permanent magnet machine design is related with only a modest reduction of the torque capability.

Fault-tolerant electric machines

There are two possible meanings of fault-tolerant electric drive systems [3]:

- a system designed to reduce the number of fault occurrences.
- a system that is able to operate even after a fault occurs, on short-term or continuously.

where the second group can be divided into two subgroups

- a PM motor drive configuration with independent phases, that may operate independently. In case of a fault in one phase, the other phases can still be operated.
- a redundant system, where the number of one or more components is extended. During healthy operation, the redundant components are totally or partially excluded.

From a practical point of view, it is not that straightforward to distinguish between a system or a machine that is designed to reduce the number of fault occurrences or is designed to be able to operate even after a fault occurs. In the case of a machine design with independent phases in order to better operate after a fault occurs, a low mutual coupling is suggested in [2] and [3]. However, the electrical insulation between phases may be increased as a consequence. An increased electrical phase separation is also mentioned in [3], both to limit the probability of fault occurrence, and as well to mitigate a fault propagation to other motor parts. Multiphase systems (a phase number greater than three) is a common approach when designing fault tolerant drive systems, considered in [2] and [4] for instance. The relative torque or power loss when one phase is lost, is in this way of course decreased, but to the cost of an increased complexity of the system. A fault-tolerant multiphase system could beneficially be designed with independent phases to be able to operate when a fault occurs, but can also be considered as a redundant system as the number of components (the phases) is increased.

From a machine design point of view, the fractional slot type of PMSM with concentrated windings has been considered as a promising alternative to achieve an independence between phases and to allow for operation during failures in a

single phase. In [5], a summary of the opportunities and challenges of the fractional slot concentrated winding PMSM can be found; some of the advantages that are mentioned are high power density, efficiency and fault-tolerance. One of the key challenges that are raised is the reduction of rotor losses since these tend to be high in fractional slot machines. Methods to reduce the rotor losses are investigated by [6], and in [7] substantial reductions of both rotor iron and permanent magnet losses are shown. The concept of fractional slot PMSM with concentrated windings are used when designing fault-tolerant multiphase machines in both [8] and [3]. The basic rules of fault-tolerant machine design are well described in [2]. The electrical, magnetic and thermal insulation between phases are important properties as well as limitation of the short circuit current.

The unbalanced conditions, associated with the operation during fault, impose additional requirements on both the controller and the converter. The control of electric machines, mainly during phase open circuit fault, has been investigated extensively in the literature. In [9] and [10], similar control methods utilizing resonant controllers are proposed but different converter topologies are considered. Two alternative control methods are suggested in [11], where feed forward terms are used to compensate for the unbalanced condition. In addition, a number of faults that occur in a PMSM drive system under field weakening operation are investigated in [12]. However, most studies are focused on the control perspective and rather simple machine models are used, often supposing a magnetic linearity. Regarding the theme of handling individual saturation levels in the different phases, there seem to be a lack of literature, according to the author's knowledge.

Purpose and main contribution of the thesis

The aim of this thesis is to design a three phase fractional slot PMSM and evaluate the possibility to operate and to deliver an acceptable quality of performance even after a fault occurs. Another part is to compare the fault-tolerant design with an existing design, where fault-tolerance was not considered in the design. The machine is to be designed fault-tolerant with a low mutual coupling between the phases and the electrical faults that are to be considered are phase open circuit fault and phase short circuit fault. This thesis is focused on the machine design perspective, not supposing a magnetic linearity, and the control and converter topologies are treated briefly only.

Some of the contributions by this licentiate thesis work can be listed as

- Development and demonstration of a machine design procedure where the relation between machine performance and material cost is considered.
- Introduction of a machine modeling technique that utilizes the weak magnetic coupling between the phases of a fault-tolerant PMSM, in order to model the unbalanced saturation associated with operation during fault more accurately.
- Quantification of the torque speed characteristics and efficiency when one PMSM is operated during phase open circuit fault or phase short circuit fault.

Chapter 1

Machine Design Modeling

This chapter provides some basic machine modeling theory from a machine design perspective. The theory is described on the basis that it is a three phase fractional slot PMSM with surface mounted permanent magnets and concentrated double-layer windings that is to be designed. However, it is possible to adapt most of the modeling techniques presented in this chapter to design of other types of machines as well.

1.1 Electric and magnetic loading

In a PMSM with surface mounted permanent magnets, where the inductance is independent of the rotor position, the torque is determined by the flux from the permanent magnets, Ψ_m , and the flux induced by the stator, $\Psi_{ind} = Li$, illustrated in Figure 1.1.

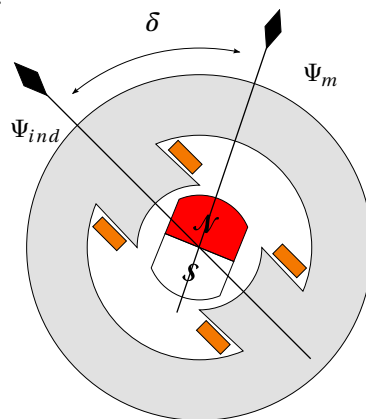


Figure 1.1: Illustration of how torque is produced between two magnetic fields.

The torque production is calculated as the cross-product of two magnetic flux vectors and it can be expressed as,

$$T = \Psi_{ind} \Psi_m \sin(\delta) \quad (1.1)$$

where δ is the angle between the vectors. In this case, the electric loading is represented by Ψ_{ind} while the magnetic loading is represented by Ψ_m . In Figure 1.2, different flux waveforms are shown together with a single tooth covering 150° electrical degrees. Figure 1.2a represents the square shaped flux density in an air-gap with surface mounted permanent magnets that covers 120 electrical degrees or $2/3$ of the pole pitch. Since the tooth covers 150 electrical degrees, the permanent magnet flux that links the tooth, Ψ_m , can be calculated as

$$\Psi_m(\theta) = \int_{\theta-75}^{\theta+75} B_m(\theta) d\theta \quad (1.2)$$

which is shown in Figure 1.2b. A tooth that covers 150° may for example be used in a fractional slot machine with 12 slots and $2p = 10$ poles, more about pole and slot combinations in Section 1.5. One can observe the low harmonic content in the flux that links a single tooth or coil.

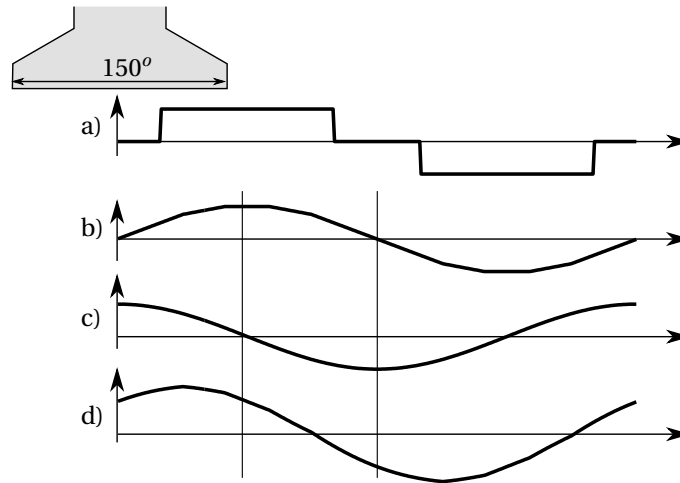


Figure 1.2: Flux wave forms; a) PM air-gap flux density. b) PM flux linked by a single coil or tooth. c) Induced flux in a single coil or tooth for maximum torque. d) Combination of PM and induced flux in a single coil or tooth

In order to maximize the torque in (1.1), the angle, δ , between the induced flux, Ψ_{ind} , and the permanent magnet flux, Ψ_m , should be 90° . The induced flux, leading the permanent magnet flux by 90° , is illustrated in Figure 1.2c. The total flux in the tooth is the sum of the permanent magnet flux and the induced flux,

$$\Psi_{tooth}(\theta) = \Psi_{ind}(\theta) + \Psi_m(\theta) = Li(\theta) + \Psi_m(\theta) \quad (1.3)$$

which is shown in Figure 1.2d. It should be noticed that the tooth carries a mix of permanent magnet flux and induced flux, although the angle between the permanent magnet flux and the current is 90° . By studying Figure 1.2 b and c, one can observe that the tooth carries a mix of the two fluxes at all angles except when one of the fluxes is crossing zero. As only one tooth is studied at the moment, one flux has its peak when the other one is zero. This is not true when the coils of several teeth are connected together and if the distribution factor is not ideal, $k_d \neq 1$. The distribution factor will be introduced later in Section 1.6. From a design point of view, this implies that flux paths must be designed with respect to the combination of permanent magnet and induced flux levels. It is also clear that any orthogonal flux vectors appearing in a phasor diagram are not independent, as they share the same non-linear iron flux paths.

1.2 Permanent magnet flux

As a simple approach, the magnetic flux distribution from a surface mounted permanent magnet can be considered as square shaped with an amplitude B_m , illustrated in Figure 1.3.

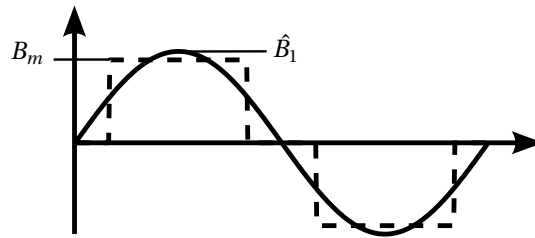


Figure 1.3: Permanent magnet air-gap flux density waveforms.

If the permanent magnets covers 120 electrical degrees or $2/3$ of the pole pitch, the peak value of the fundamental, \hat{B}_1 , can be calculated as,

$$\hat{B}_1 = \frac{4\sqrt{3}}{2\pi} B_m \quad (1.4)$$

A permanent magnet that covers 2/3 of the pole pitch is often considered a suitable choice, due to the utilization of the permanent magnet flux and to achieve a low cogging torque. If the reluctance of the iron paths and the leakage flux are neglected, the required length of the permanent magnets, l_{pm} , is expressed as

$$l_{pm} = \frac{\mu l_g}{\frac{B_r}{B_m} - 1} \quad (1.5)$$

where l_g is the air-gap length, μ the relative permeability of the permanent magnets and B_r is the residual flux density of the permanent magnets.

1.3 Core loss and core geometry

Accurate computation of the iron or core losses is a complicated task. The iron losses are often separated into three parts:

- Hysteresis losses
- Eddy current losses
- Excess losses

A number of iron loss models for electrical machines are presented and compared in [13]. One approach is to formulate an expression with three terms, one for each loss part,

$$P_{core} = c_{hyst} f \hat{B}^2 + c_{ec} f^2 \hat{B}^2 + c_{exc} f^{1.5} \hat{B}^{1.5} \quad (1.6)$$

where P_{core} is the core loss volume density and the coefficients are empirical factors. If only considering the hysteresis and eddy current losses at a single frequency,

$$P_{Fe} \propto B^2 V \quad (1.7)$$

where P_{Fe} is the total loss in the volume, V , and B is the flux density. If flux is floating a distance, X_0 , from the left to the right in the geometry illustrated in

Figure 1.4 and the flux is assumed to be uniform distributed along a vertical segment,

$$B = \frac{\phi}{A} \quad (1.8)$$

where ϕ is the total flux that crosses each segment and A is the one-dimensional area of a segment in vertical direction.

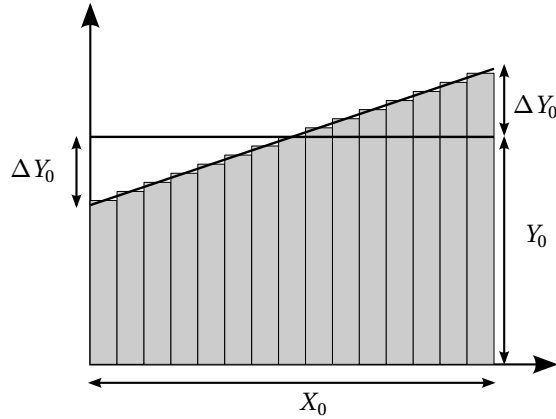


Figure 1.4: Illustration of a segmented flux path volume.

The volume of a single element, V , is the horizontal thickness of a segment, l , multiplied by the one-dimensional area, A . Then, (1.7) and (1.8) together gives,

$$P_{Fe} \propto \frac{1}{A^2} l A = \frac{l}{A} \quad (1.9)$$

which implies that the reluctance, \mathfrak{R} , of the path X_0 , when carrying the total flux ϕ , should be minimized in order to minimize the core loss since,

$$\mathfrak{R} = \frac{l}{\mu A} \quad (1.10)$$

For a flux path of the length X_0 and the constant core volume $V = X_0 \cdot Y_0$, the variable ΔY_0 is used to vary the shape of the geometry. The reluctance, when dividing the flux path into k segments, can be expressed as

$$\mathfrak{R} = \frac{1}{\mu} \sum_{n=1}^k \frac{X_0}{k(Y_0 - \Delta Y_0) + 2\Delta Y_0 n} \quad (1.11)$$

The reluctance in (1.11) has a minimum for $\Delta Y_0 = 0$, corresponding to a constant cross-sectional area along the flux path and evenly distributed flux. The reasoning in this section together with knowledge about how the flux is divided between different paths can be applied when dimensioning the flux paths. It is beneficial to aim for constant flux densities along flux paths.

1.4 Thermal conductivity of the winding mix

When modeling the thermal characteristics of the windings, the copper conductors and the impregnation material between the conductors are often treated as a mix material with an equivalent thermal conductivity. As the thermal conductivity of copper is much higher than for the impregnation material, 1:1833 in [14], both the conductivity of the impregnation material and the distribution of the copper wires are of great importance when determining an equivalent thermal conductivity of the material mix. Conductors of the same size placed in a hexagon pattern and a square pattern with the same fill-factor are illustrated in Figure 1.5. The hexagon pattern gives a longer shortest path between the conductors which results in a lower equivalent thermal conductivity compared to the square pattern distribution, when the same fill-factor is considered.

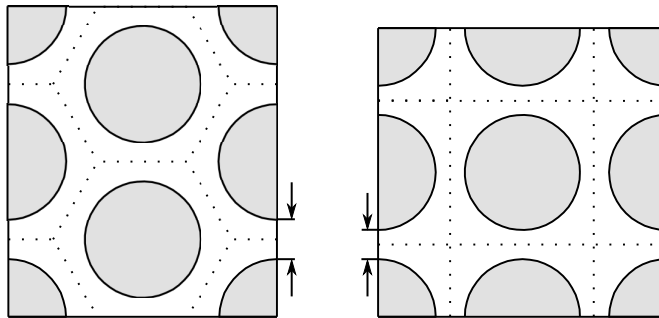


Figure 1.5: Hexagon and square pattern distribution of conductors, the conductors have the same size and the same fill-factors are used.

Using FEA, equivalent thermal conductivity that are calculated for hexagon and square pattern distributions as function of the copper fill-factor are presented in Figure 1.6 and Figure 1.7, for two different values of thermal conductivity of the impregnation material. It can be seen that the equivalent thermal conductivities increase dramatically when the fill-factors are approaching the theoretical maximal fill-factors, $\frac{\pi}{4} \approx 0.79$ and $\frac{\pi}{2\sqrt{3}} \approx 0.91$, for square and hexagon distribution respectively. The figures show clearly the impact of the conductor distribution and the thermal conductivity of the impregnation material for all combinations. The impact of the fill-factor on the relative increase of the equiva-

lent thermal conductivity is significant at already very high fill-factors. From a strictly thermal perspective it's therefore beneficial to aim for even a slight increase of an already very high fill-factor.

Interesting improvements of the performance at the thermal limit for two segmented PMSMs using wound windings (fill-factor of 61%) and using pre-pressed windings (fill-factor of 78%) are presented in [15]. In [16], thermal properties for a mix of Litz wire and impregnation material, using two impregnation techniques, are derived experimentally. The first sample, that was varnish dipped, shows an equivalent thermal conductivity of 1.2-1.6 W/(m·K) while the second sample, that was epoxy impregnated using a vacuum chamber, shows an equivalent thermal conductivity of 2.9-7.4 W/(m·K).

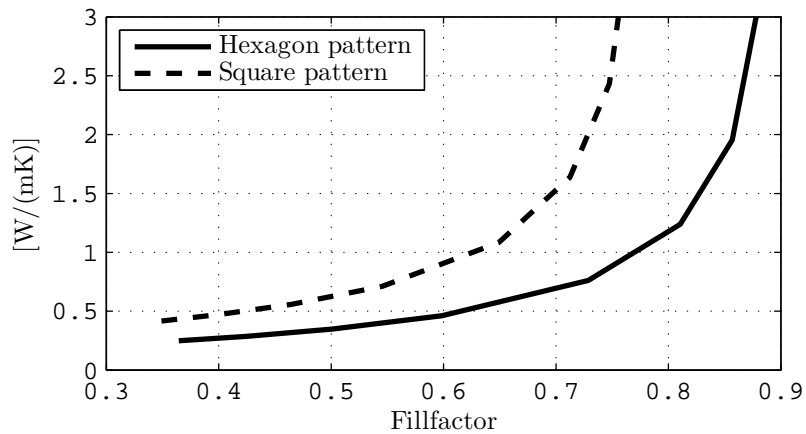


Figure 1.6: Equivalent thermal conductivity for winding mix for an impregnation conductivity of 0.2 W/m·K.

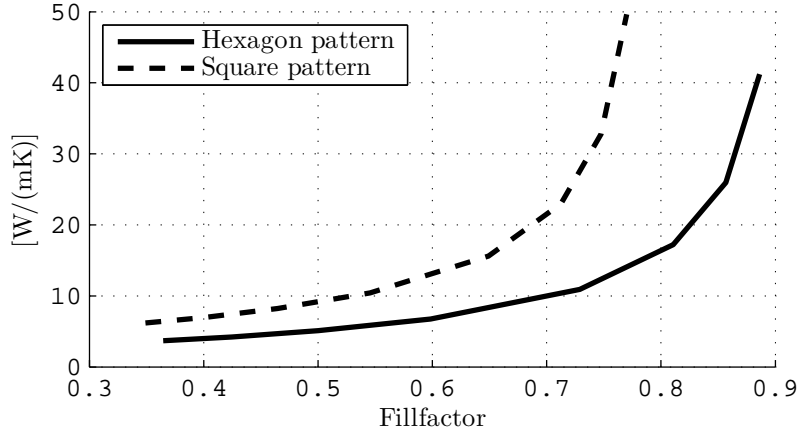


Figure 1.7: Equivalent thermal conductivity for winding mix for a impregnation conductivity of 3 W/m·K.

1.5 Pole and slot combinations

For a three phase machine, $m = 3$, the total number of poles, $2p$, should be as close as possible to the number of slots, Q_s , in order to maximize the magnetic flux linkage. Equal numbers or a pole pitch of one, $\tau = \frac{Q_s}{2p} = 1$, can't be used if the motor is to be able to produce torque in all rotor positions. The feasible pole and slot combinations are usually described by

$$Q_s = 2p \pm 1 \text{ or } 2p \pm 2 \quad (1.12)$$

where Q_s must be a multiple of 3 for a three phase machine. Furthermore, for a three phase machine, the mechanical displacement of the phases must result in an electrical displacement of 120 degrees of the phases, which gives that

$$\frac{360p}{3} = \pm 360k + 120 \quad k = 0, 1, 2, \dots \quad (1.13)$$

All feasible combinations, up to $p = 14$, derived from (1.12) and (1.13) are listed in Table 1.1. It can be noted in Table 1.1 that no combinations where p is a multiple of 3 exist, which is a consequence of (1.12). Further, there is only one combination for $p=1$ as Q_s must be a multiple of 3 for a three phase machine.

Q_s and p for a given combination of Q_s/p can be multiplied by a positive integer to get a new feasible combination.

Table 1.1: Feasible pole and slot combinations for a 3-phase machine.

p	$Q_s = 2p \pm 1$	$Q_s = 2p \pm 2$
1	3	-
2	3	6
4	9	6
5	9	12
7	15	12
8	15	18
10	21	18
11	21	24
13	27	24
14	27	30

Using a $Q_s = 2p \pm 1$ combination results in an odd number of coils per phase for a concentrated double-layer wound machine, which will limit the number of possible series and parallel connection of the coils. A $Q_s = 2p \pm 1$ combination gives also lower number of slots and thereby larger windings for a given pole number.

1.6 Winding factor

The winding factor describes how well flux of a specific harmonic from the rotor side links a phase winding and is determined by the Q_s/p combination and the winding configuration. It is defined as the pitch factor multiplied by the distribution factor [17] which can be seen in (1.14).

$$k_{wn} = k_{pn} k_{dn} \quad (1.14)$$

where the pitch factor, k_{pn} , describes how well flux from a given harmonic links a single coil or tooth. The pitch factor for any Q_s/p combination can be expressed according to

$$k_{pn} = \sin\left(\frac{n\pi p}{Q_s}\right) \quad (1.15)$$

where $n = 1$ corresponds to the fundamental of each combination [18]. The distribution factor, k_{dn} , is used to include the phase shift between the flux linkage in each coil when summing up the contribution for a given harmonic in a phase. Hence, the formulation of distribution factor is determined by both the Q_s/p combination and the winding configuration. For concentrated double-layer windings k_{dn} can be expressed as [18]

$$k_{dn} = \frac{\sin(\frac{n\pi}{2m})}{z \sin(\frac{n\pi}{2mz})} \quad (1.16)$$

where n is the harmonic number, m is the number of phases and z is the number of coils in a group. The number of coils in a group can be calculated as,

$$z = \frac{Q_s}{mF} \quad (1.17)$$

where F is the greatest common divisor (GCD) of the number of poles, $2p$, and the number of slots, Q_s .

$$F = GCD(2p, Q_s) \quad (1.18)$$

Winding factors for feasible $Q_s = 2p \pm 2$ combinations up to $p = 13$ are shown in Table 1.2.

Table 1.2: Winding factors for the 1st to the 13th harmonic for feasible $Q_s = 2p \pm 2$ combinations up to $p = 10$.

Q_s/p	Harmonic number												
	1	2	3	4	5	6	7	8	9	10	11	12	13
6/2	0.87	0.87	0	-0.87	-0.87	0	0.87	0.87	0	-0.87	-0.87	0	0.87
6/4	0.87	-0.87	0	0.87	-0.87	0	0.87	-0.87	0	0.87	-0.87	0	0.87
12/5	0.93	0.43	-0.50	-0.43	0.07	0	-0.07	0.43	0.50	-0.43	-0.93	0	0.93
12/7	0.93	-0.43	-0.50	0.43	0.07	0	-0.07	-0.43	0.50	0.43	-0.93	0	0.93
18/8	0.95	0.29	-0.58	-0.29	0.14	0	0.06	0.29	0	-0.29	-0.06	0	-0.14
18/10	0.95	-0.29	-0.58	0.29	0.14	0	0.06	-0.29	0	0.29	-0.06	0	-0.14
24/11	0.95	0.22	-0.60	-0.22	0.16	0	0.10	0.22	-0.10	-0.22	0.02	0	-0.02
24/13	0.95	-0.22	-0.60	-0.22	0.16	0	0.10	-0.22	-0.10	0.22	0.02	0	-0.02

1.7 MMF time and space harmonics

Rotor losses caused by the induced magneto motive force (MMF) wave is mentioned as one of the key challenges for fractional slot machines with concentrated windings in [5]. As a first step the rotor losses can be lowered if the source is minimized by a careful choice of pole slot combinations to achieve a favorable MMF wave in the air-gap, why the calculation of time and space harmonics is of great importance. For a given pole/slot combination, the impact of the harmonics in the MMF wave can be affected by geometry and material properties. It is possible to increase the air-gap length and introduce segmentation of the rotor parts in order to prevent the induction of eddy currents on the rotor side. The correlation between pole/slot combinations and rotor losses using different air-gap lengths and rotor surface materials are investigated extensively in [6]. The basic theory of how to analytically calculate the theoretical induced MMF harmonics is very well described in [19] for example. In this section a conceptual explanation follows, based on an example of the $Q_s = 12$ machine.

The MMF wave that is induced in the air-gap when the stator is excited by current can be described by means of MMF time and space harmonics,

$$F(t, \theta) = \sum_n \sum_m F_{nm} \sin(m\omega t \pm n\theta + \beta_{mn}) \quad (1.19)$$

where F_{nm} is time m:th order and space n:th order MMF magnitude. The stator together with its winding configuration is illustrated in the bottom of Figure 1.8. Just above the stator, the ideal square wave MMF-wave is plotted together with the dotted MMF-wave built up by the first seven non-zero components of space harmonics. The space harmonic order is defined so that the fundamental period is 2π in mechanical angle. The first seven non-zero components (1, 5, 7, 11, 13, 17, 19) are shown with their respective magnitude and phase above the full MMF-wave. It can be seen that the 5th and the 7th harmonics are of the greatest amplitude, verifying that $Q_s = 12$ stator is suitable for $p = 5$ and $p = 7$, previously shown in Table 1.1.

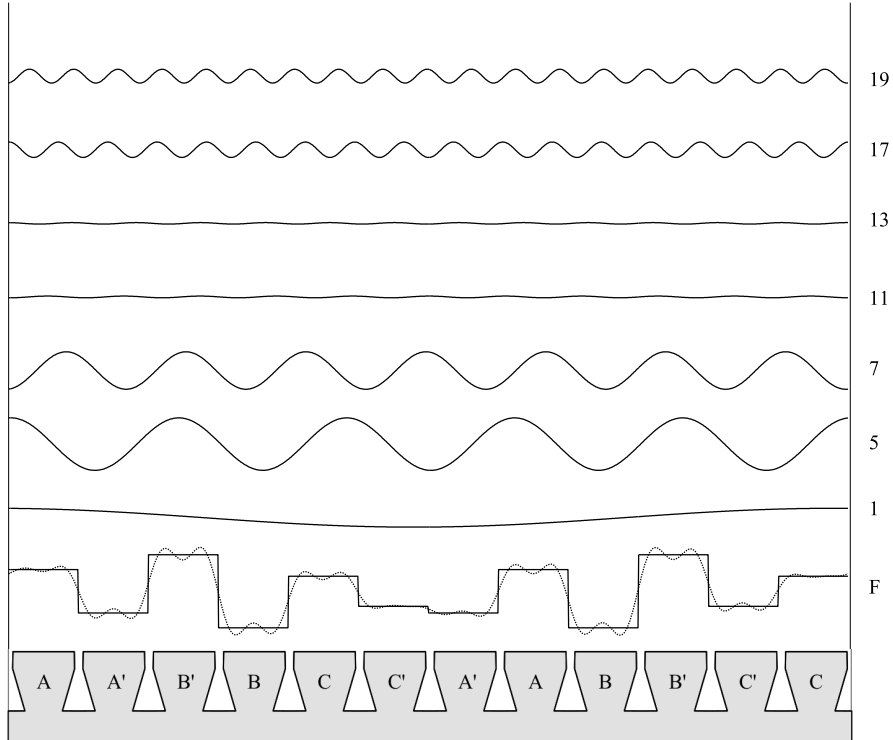


Figure 1.8: MMF-wave and its harmonic content in the air-gap of a $Q_s = 12$ machine.

The MMF harmonics rotate in the air-gap with different speeds, as all harmonics travel one wave-length during one period, the mechanical speed of the n :th MMF harmonic in the stator reference frame can be calculated as [6]

$$\omega_{ns} = \frac{\omega}{\text{sign} \cdot n} \quad (1.20)$$

where sign is either +1 or -1 depending on travel-direction of the n :th harmonic. The sign-function is defined as two series of harmonics that travel in the opposite direction [6]

$$n = 1 + 3k \quad k = 0, 1, 2, \dots \quad (1.21)$$

and

$$n = 2 + 3k \quad k = 0, 1, 2, \dots \quad (1.22)$$

A positive sign is conventionally assigned to the series containing the main harmonic ($n = p$). The harmonic content of the MMF-wave in a $p = 5$ and $p = 7$ machine respectively are shown in Figure 1.9. The amplitudes are expressed in relation to the fundamentals which corresponds to the red bar. Positive values indicate that the harmonics are traveling in the same direction as the fundamental and negative values in the opposite direction.

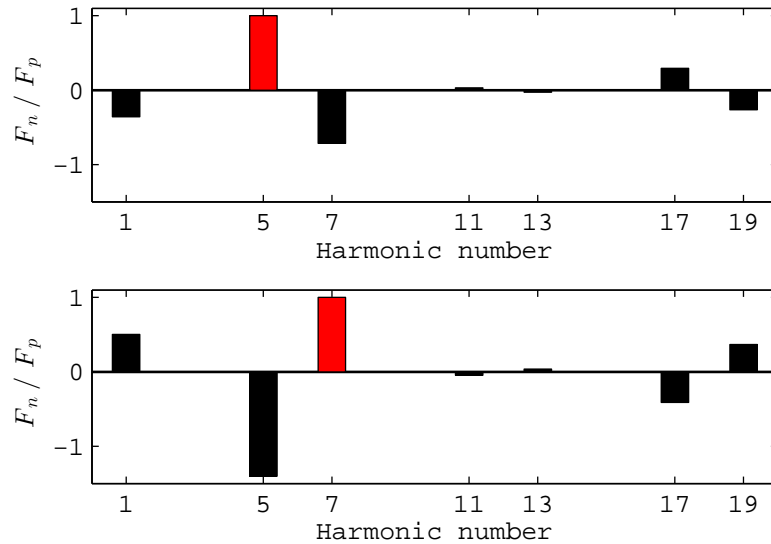


Figure 1.9: Harmonic content in the air-gap for the $p = 5$ and $p = 7$ machine respectively, the amplitudes are related to the fundamentals which corresponds to the red bars.

When it comes to the losses on the rotor side due to the MMF harmonics in the air-gap, it is the traveling speed of the n :th harmonic relative to the fundamental, $n = p$, that is of interest. Ideally, the fundamental will travel with the same speed as the rotor and only induce a constant magnetic flux seen from the rotor. The rest of the harmonics will travel with a speed that is not the same as the rotor and hence introduce an alternating magnetic flux that may cause losses on the rotor side. As consequence, the rotors of the $p = 5$ and the $p = 7$ machines

will experience different harmonics when using the same stator, $Q_s = 12$. The frequency of the MMF seen from the rotor side can be expressed as

$$f_{rn} = f \left| \text{sign} - \frac{n}{p} \right| \quad (1.23)$$

Figure 1.10 shows the relative frequency of the MMF harmonics on the rotor side. It can be noticed that some MMF harmonics have the same relative frequency on the rotor side, the 1st and the 11th for the $p=5$ for instance. This since the 1st rotate in the opposite direction related to the fundamental ($5-(-1)=6$) while the 11th rotate in the same direction as the fundamental ($11-5=6$).

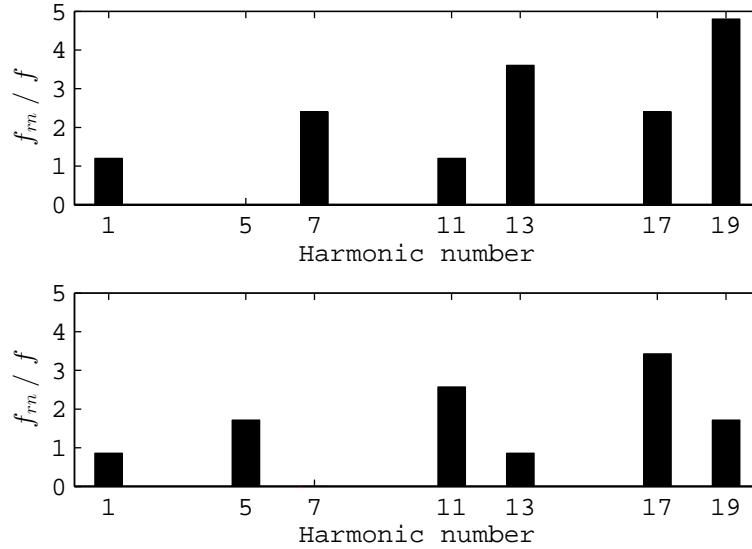


Figure 1.10: Relative frequency of the MMF harmonics on the rotor side. The frequency of the fundamental $n = p = 5$ and $n = p = 7$ equals zero for both configurations.

The rotor losses caused by the MMF harmonics for different pole slot combinations are determined by the presence of harmonics, the amplitude of the harmonics, the relative frequency of the MMF harmonics on the rotor side together with the harmonic number (physical wave length in relation to the rotor geometry). Subharmonics, $n < p$, especially $n = 1$ which is present for both the machines in Figure 1.9 might be considered as extra critical as a wave length covers the whole air-gap. An MMF harmonic covering the whole air-gap means

a flux path across the whole rotor and potentially deep flux penetration of the rotor structure. A strategy to reduce the flux produced by an undesirable harmonic, and thereby the losses, is to increase the reluctance of the flux path used by that specific harmonic without affecting the flux path of the fundamental. Introduction of different flux barriers to prevent flux caused by subharmonics are presented in [20] and [7].

1.8 Inductance calculation

One way of analytically calculating the flux and the inductance of an electric machine is to create a reluctance circuit; a reluctance circuit of a 12 slot machine is shown in Figure 1.11. Different paths of the magnetic circuit of the machine are lumped together into their corresponding reluctance elements. Each reluctance element is determined by the geometric properties of the machine parts together with its material properties. The reluctance circuit is then excited by magneto motive forces (MMFs) corresponding to the product of the current and the number of turns in the coils.

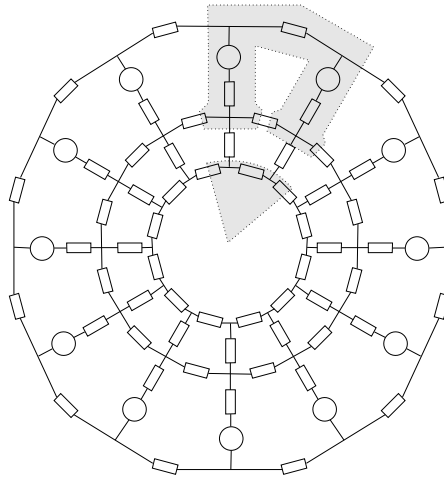


Figure 1.11: A reluctance circuit that represents a complete 12 slot machine.

A column vector, Φ , that consists of the magnetic flux in the loops of the reluctance circuit can be calculated as

$$\Phi = \mathfrak{R}^{-1} \mathbf{MMF} \quad (1.24)$$

where \mathfrak{R} is a matrix that describes the reluctance circuit and MMF is a vector that corresponds to the MMF-sources in each flux loop in Figure 1.12. The flux in each tooth can then be calculated as the difference between the fluxes in the two loops on each side of the tooth. In Figure 1.12, the reluctance circuit is built up by five different reluctance elements. A similar reluctance circuit and analytically expressions for the reluctance element are presented in [21].

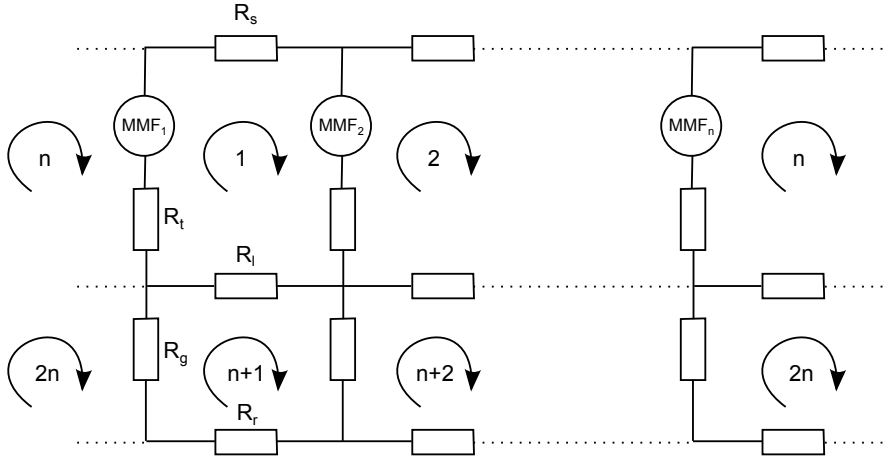


Figure 1.12: Schematic representation of a reluctance circuit for a machine with an arbitrary number of slots, $Q_s = n$.

The reluctance matrix can be expressed as

$$\mathfrak{R} = \begin{bmatrix} (\sum_{k=1}^{2n} R_{1,k}) & -R_{1,2} & -R_{1,3} & \cdots & -R_{1,2n} \\ -R_{2,1} & (\sum_{k=1}^{2n} R_{2,k}) & -R_{2,3} & \cdots & -R_{2,2n} \\ \vdots & \vdots & \vdots & \ddots & \vdots \\ -R_{2n,1} & -R_{2n,2} & -R_{2n,3} & \cdots & (\sum_{k=1}^{2n} R_{2n,k}) \end{bmatrix} \quad (1.25)$$

where $R_{k,l}$ is the reluctance element that serves as a path for the flux both for the flux in loop k and loop l . Therefore, $R_{1,2} = R_t$, since the element R_t is a path in both loop 1 and loop 2, as seen in Figure 1.12. As a second example; $\sum_{k=1}^{2n} R_{1,k} = R_s + R_t + R_l + R_r$.

The n first elements in the MMF column vector can then be written as

$$\mathbf{MMF}(1:n) = \begin{bmatrix} MMF_1 - MMF_2 \\ MMF_2 - MMF_3 \\ \vdots \\ MMF_{n-1} - MMF_n \\ MMF_n - MMF_1 \end{bmatrix} \quad (1.26)$$

where the winding direction or the coil configuration of each coil with respect to the direction of the flux loop must be taken into account. The rest of the MMF column vector is zero, $\mathbf{MMF}(n+1:2n) = 0$, as there are no coils or current excitation on the rotor side.

The calculated flux in each tooth can now be summed up for each phase to calculate the flux linkage in the corresponding phases. The self-inductance of phase a relates the flux of phase a, linking the coils of phase a and the current in phase a as follows

$$L_{aa} = \frac{\Lambda_{aa}}{i_a} \quad (1.27)$$

The mutual inductance between phase a and b relates the flux from phase a, linking the coils of phase b and the current in phase a

$$L_{ab} = \frac{\Lambda_{ab}}{i_a} \quad (1.28)$$

Chapter 2

Dynamic Modeling of PMSMs

This chapter deals with the the dynamic modeling of PMSMs under balanced and unbalanced or faulty conditions. Although this licentiate thesis focuses on the design of a fault-tolerant PMSM, the unbalanced conditions impose additional requirements of the controller and the converter. Both a controller and some converter topologies that can handle the unbalanced operation are therefore presented. The reader is expected to be familiar with general machine modeling and the transformations between the different reference frames that are associated with both machine modeling and control, which are well described in [22] for example.

2.1 Basic 3ph-model

The electrical equations, expressing the phase voltages of a three phase PMSM can be written on matrix form as

$$\begin{bmatrix} v_a \\ v_b \\ v_c \end{bmatrix} = \begin{bmatrix} L_{sa} & L_{sab} & L_{sac} \\ L_{sab} & L_{sb} & L_{sbc} \\ L_{sac} & L_{sbc} & L_{sc} \end{bmatrix} \frac{d}{dt} \begin{bmatrix} i_a \\ i_b \\ i_c \end{bmatrix} + \begin{bmatrix} R_s & 0 & 0 \\ 0 & R_s & 0 \\ 0 & 0 & R_s \end{bmatrix} \begin{bmatrix} i_a \\ i_b \\ i_c \end{bmatrix} + \begin{bmatrix} e_a \\ e_b \\ e_c \end{bmatrix} \quad (2.1)$$

where e_a , e_b and e_c are the back EMF terms of each phase. If the flux from the permanent magnets are considered to be sinusoidal and symmetrically placed towards each other, the back EMF terms can be formulated as

$$\begin{bmatrix} e_a \\ e_b \\ e_c \end{bmatrix} = \omega \Psi_m \begin{bmatrix} \cos(\theta) \\ \cos(\theta - \frac{2\pi}{3}) \\ \cos(\theta - \frac{4\pi}{3}) \end{bmatrix} \quad (2.2)$$

where ω is the electric angular frequency and Ψ_m is the magnitude of the flux linkage in a phase. Further, the self inductance of the phases are equal and they can be denoted

$$L_{sa} = L_{sb} = L_{sc} = L \quad (2.3)$$

Also the mutual coupling between all phases are the same and it can be denoted

$$L_{sab} = L_{sac} = L_{sbc} = M \quad (2.4)$$

For a balanced three phase system where $i_a + i_b + i_c = 0$ and utilizing $L_s = L - M$, (2.1) can be rewritten as

$$\begin{bmatrix} v_a \\ v_b \\ v_c \end{bmatrix} = \begin{bmatrix} L_s & 0 & 0 \\ 0 & L_s & 0 \\ 0 & 0 & L_s \end{bmatrix} \frac{d}{dt} \begin{bmatrix} i_a \\ i_b \\ i_c \end{bmatrix} + \begin{bmatrix} R_s & 0 & 0 \\ 0 & R_s & 0 \\ 0 & 0 & R_s \end{bmatrix} \begin{bmatrix} i_a \\ i_b \\ i_c \end{bmatrix} + \begin{bmatrix} e_a \\ e_b \\ e_c \end{bmatrix} \quad (2.5)$$

For a machine without rotor saliency, the inductance is not dependent on the rotor position and no reluctance torque can be created. Hence, the electrodynamic torque can be expressed as

$$T_e = \frac{i_a e_a}{\Omega} + \frac{i_b e_b}{\Omega} + \frac{i_c e_c}{\Omega} \quad (2.6)$$

where Ω represents the mechanical angular frequency.

2.2 Flux model in the rotating dq-reference frame

In the rotating dq reference frame, the stator voltage of a PMSM can be expressed as

$$u_d = R_s i_d + L_d \frac{di_d}{dt} - \omega L_q i_q \quad (2.7)$$

$$u_q = R_s i_q + L \frac{di_q}{dt} + \omega L_d i_d + \omega \Psi_m \quad (2.8)$$

where only the fundamental frequency component is considered and the permanent magnet flux is oriented in the direct axis. The electrodynamic torque can be written as

$$T_e = \psi_d i_q - \psi_q i_d \quad (2.9)$$

If the flux components are expressed as $\psi_d = \Psi_m + L_d i_d$ and $\psi_q = L_q i_q$, the torque equation (2.9) can be rewritten as

$$T_e = \Psi_m i_q + (L_d - L_q) i_d i_q \quad (2.10)$$

which is a widely used expression. Using this model for a non-linear machine, it is problematic to divide the direct axis flux, ψ_d , into its PM flux component, Ψ_m and its induced flux component, $L_d i_d$. Both Ψ_m and $L_d i_d$ share the same non-linear flux paths, as previously shown in Figure 1.2 in Section 1.1. Consequently, both Ψ_m and L are functions of the currents, i_d and i_q , and it is thereby possible to divide ψ_d in an infinite number of combinations of Ψ_m and $L_d i_d$ if no further assumptions are introduced.

Another possibility is to model the PMSM based on the flux including all harmonics without dividing the direct axis flux into PM and induced flux. The flux in the direct and quadrature axis is a function of the currents and the rotor position respectively

$$\psi_d = \psi_d(i_d, i_q, \theta) \quad (2.11)$$

$$\psi_q = \psi_q(i_d, i_q, \theta) \quad (2.12)$$

where the rotor angle, θ , must be varied within an interval determined by the pole/slot combination and winding configuration. Equation (2.11) and (2.12) are rather impractical since the fluxes vary in three dimensions. If only considering the fundamental frequency and a steady-state operating point, (2.7) and (2.14) can be rewritten as

$$u_d = R_s i_d - \omega \Psi_q \quad (2.13)$$

$$u_q = R_s i_q + \omega \Psi_d \quad (2.14)$$

where both Ψ_d and Ψ_q represent the amplitudes of the fundamental component of the flux linkage in the direct and quadrature axis respectively. A set of Ψ_d and Ψ_q as function of i_d and i_q can be calculated by means of FEA, using (2.13) and (2.14). Thus, the fundamental phase voltage at a steady-state operating point can be found accurately.

2.3 Basic modeling of chosen faults

The three phase model presented in (2.1) can be written on the general state space form

$$\dot{x} = Ax + Bu \quad (2.15)$$

$$y = Cx + Du \quad (2.16)$$

In the state space model of the machine, the currents represent the states, the current derivatives the state derivatives, while the input voltage is used as input and it becomes

$$\frac{d\mathbf{i}}{dt} = -inv(\mathbf{L})\mathbf{R}\mathbf{i} + inv(\mathbf{L})\mathbf{v} - inv(\mathbf{L})\mathbf{e} \quad (2.17)$$

The corresponding \mathbf{A} and \mathbf{B} can then be expressed as

$$\mathbf{A} = -inv(\mathbf{L})\mathbf{R} \quad (2.18)$$

$$\mathbf{B} = inv(\mathbf{L}) \quad (2.19)$$

The three phase model can then be implemented as follows

$$\frac{d}{dt} \begin{bmatrix} i_a \\ i_b \\ i_c \end{bmatrix} = \mathbf{A} \begin{bmatrix} i_a \\ i_b \\ i_c \end{bmatrix} + \mathbf{B} \begin{bmatrix} v_a \\ v_b \\ v_c \end{bmatrix} - \mathbf{B} \begin{bmatrix} e_a \\ e_b \\ e_c \end{bmatrix} \quad (2.20)$$

where

$$\mathbf{A} = \begin{bmatrix} A_{11} & A_{12} & A_{13} \\ A_{21} & A_{22} & A_{23} \\ A_{31} & A_{32} & A_{33} \end{bmatrix} \quad (2.21)$$

and

$$\mathbf{B} = \begin{bmatrix} B_{11} & B_{12} & B_{13} \\ B_{21} & B_{22} & B_{23} \\ B_{31} & B_{32} & B_{33} \end{bmatrix} \quad (2.22)$$

which is referred to in the following sections, where it has been manipulated to include phase open and phase short circuit faults.

2.3.1 Phase short circuit

The suggested phase short circuit fault manipulation of (2.20) is probably the most straightforward. The terminal phase voltage of the faulty phase, v_i , is simply put to zero. Characteristics of the short circuit connection might be added by manipulation of the R and L matrices if desired.

2.3.2 Phase open circuit

Two different ways of phase open circuit manipulation are presented. The first changes instantaneously from normal operation to phase open circuit operation while the second takes the transition into account.

State and energy removed

In the most simple approach, the simulation stops when a fault occurs. The states in the machine model (and possible other states such as values in the integrator parts of controllers) are saved. The model is then changed, the state that represents the faulty phase is removed. The saved states are then used as

initial conditions when starting the simulation of the new model that represents the characteristics after the fault occurred. As a consequence, energy is removed when the state corresponding to current in the faulty phase is removed.

State and energy conserved

As a second approach, the state corresponding to the current in the faulty phase is controlled to zero; instead of just put the current in the faulty phase to zero and thereby removing the energy instantaneously. From a simulation perspective it is beneficial to control the current to interrupt like a first order system, see Figure 2.1. The voltage that has to build up over the phase winding is calculated and used as input signal to the state space model, where all states still are remaining.

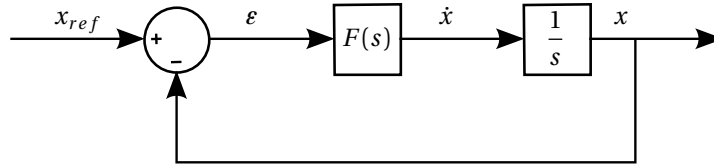


Figure 2.1: Illustration of how the derivative of the state can be controlled.

To get the behavior of a first order system, from the state reference, x_{ref} , to the state value, x , it can be shown that $F(s) = \alpha$, where α is the bandwidth of the first order system. The state derivative, representing the faulty phase, in the state space model can then be expressed as

$$\dot{x} = \alpha(x_{ref} - x) \quad (2.23)$$

when a fault occurs. The voltage that must build up over the phase winding (phase c is used in this case) is calculated as

$$v_c = \frac{\alpha(0 - i_c) - A(3, 1:3)i(1:3) - B(3, 1:2)u(1:2) + B(3, 1:3)e(1:3)}{b(3,3)} \quad (2.24)$$

2.4 Control

This section presents the two controllers, in the rotating dq0 reference frame, that are used in this thesis. The ordinary PI controller, that are suitable for balanced three phase control are not explained in detail as it is very well established within electric machine control. Adding a resonant controller in parallel with an existing PI controller is proposed when operating the machine under faulty and unsymmetrical conditions.

2.4.1 Ordinary PI controller

When the ordinary PI controller is used in the dq0 reference frame, the rotating three phase quantities are transformed to stationary quantities in the rotating dq0 reference frame via the stationary $\alpha\beta 0$ reference frame. In case of a balanced three phase system in steady-state, all the dq0-components will appear as DC-values which the PI controller is well adapted for. The PI controller is represented as the lower part in the combined resonant and PI controller in Figure 2.2 in section 2.4.2.

2.4.2 Resonant and PI controller

In case of an unbalanced three phase system, as will appear under a phase open circuit and short circuit fault condition, the transformed direct, quadrature and zero sequence components of the three phase quantities will not all be constant values at the same time. As a result, one or several of the dq0-components will be oscillating. Therefore, the ordinary PI controller, that greatly can handle the transformed DC-values under normal conditions, is not a good choice to control the machine currents under faulty conditions. One method, suggested by [9], is to add a resonant controller in parallel with the ordinary PI-controller, which is shown in Figure 2.2.

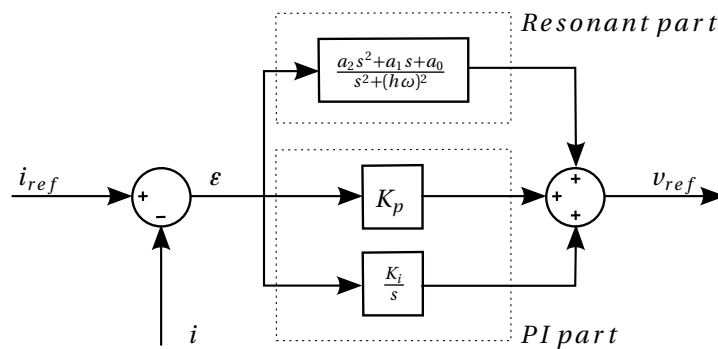


Figure 2.2: Combined resonant and PI controller

In case of a machine with surface mounted permanent magnets and no rotor saliency, no reluctance torque is expected as $L_d = L_q$, and it is only necessary to keep the torque producing q-component of the current constant. On the other hand, for a machine with a difference between the direct and quadrature axis inductance it is also necessary to hold the d-component of the current constant. The proposed current controller will force both the q and the d components of the current to constant values, while the zero sequence component that does not produce torque is left oscillating.

2.5 Converter limitations

Using the ordinary three leg converter that is shown in Figure 2.3a, it is not possible to control the phase currents individually in case of a phase open circuit or a phase short circuit. The current into one of the remaining phases must equal the current that goes out from the second healthy phase. Three alternative converter topologies are therefore described briefly.

The converter topology illustrated in Figure 2.3b is equipped with a fourth leg that is connected to the star of the Y-connected phases. Thanks to the fourth leg, it is possible to control the remaining phases individually if one phase is lost. A second example of connecting the star point is shown in Figure 2.3c, where it is made possible to connect the star point to the middle of the DC-link by an additional switch or relay. This configuration saves one switch and the control of the fourth phase leg compared to the solution in Figure 2.3b, as the switch is constantly closed in case of a fault. This configuration has been utilized in [10].

The last example is the six leg converter that can be seen in Figure 2.3d, where each phase winding is connected to its own H-bridge. The six leg converter is considered in [9] for instance. The six leg converter offers the greatest degree of freedom, but the number of switches and phase cables are doubled compared to the ordinary three phase converter. For the same power level, the product of the number of switches and the rating of each switch ($V \cdot I$) is increased by a factor $2/\sqrt{3} \approx 1.15$ for the six leg inverter compared with an ordinary three leg converter [3]. In the same manner as in [3], it can be shown that total cross-sectional area of the copper in the six cables of a six leg converter is also increased by a factor $2/\sqrt{3} \approx 1.15$ compared to the three cables of an ordinary three leg converter, when the same DC-link voltage level and current density are considered. An advantage among other, is that a phase can be completely short circuited to limit the short circuit current in case of a turn to turn short circuit fault, while it is still possible to control the two remaining phases.

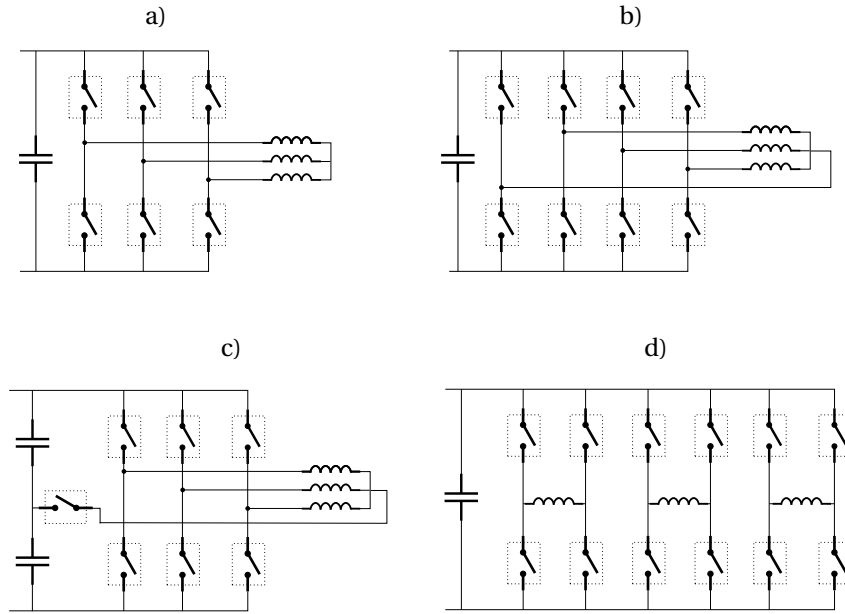


Figure 2.3: Four different converter topologies.

The three colored vectors on the left hand side in Figure 2.4 represent the physical arrangement of the windings in a three phase machine, distributed 120 electrical degrees apart. If they are denoted $\bar{\mathbf{x}}_i$, the orientation of each phase can be expressed as

$$\bar{\mathbf{x}}_a = e^{j0} \quad (2.25)$$

$$\bar{\mathbf{x}}_b = e^{j2\pi/3} \quad (2.26)$$

$$\bar{\mathbf{x}}_c = e^{-j2\pi/3} \quad (2.27)$$

The three phase currents that are sinusoidal and 120 electrical degrees apart can be written as

$$I_a = \hat{I} \sin(\omega t) \quad (2.28)$$

$$I_b = \hat{I} \sin(\omega t - 2\pi/3) \quad (2.29)$$

$$I_c = \hat{I} \sin(\omega t + 2\pi/3) \quad (2.30)$$

and they are shown in the right hand side of Figure 2.4. Using the physical arrangement of the windings and the current waveforms together, the induced flux from the stator can be expressed as

$$\bar{\Psi}_s = L(\bar{x}_a I_a + \bar{x}_b I_b + \bar{x}_c I_c) \quad (2.31)$$

where L is the phase inductance and there is no mutual inductance between the phases. $\bar{\Psi}_s$ is a vector, with constant magnitude, that rotates with the electric frequency and follows the dotted circle shown in Figure 2.4.

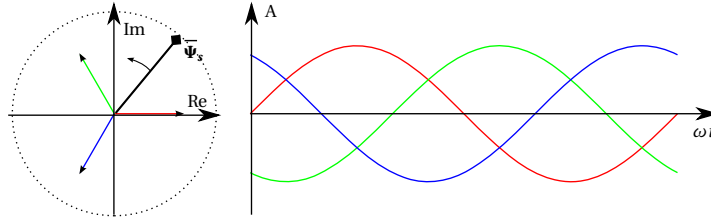


Figure 2.4: Normal operation, phase shift of 120 electrical degrees between the phase currents.

If one phase is lost and the two remaining currents are left unaltered, the induced flux, $\bar{\Psi}_s$, will rotate with the electric frequency and a time varying amplitude as illustrate in Figure 2.5. If considering the physical arrangement of the windings in Figure 2.5, it can be seen directly that there is only one phase that can induce flux in the direction of the imaginary axis.

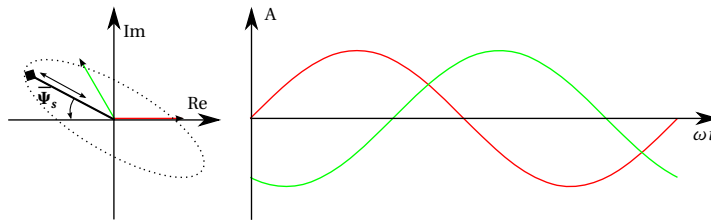


Figure 2.5: One phase lost, phase shift of 120 electrical degrees between the two remaining phase currents.

The maximum flux that can be induced in the direction of the imaginary axis is therefore $imag(\bar{x}_b I_b L) = \hat{I} \cdot \cos(\pi/6) \cdot L$. It can easily be shown that the bal-

anced three phase system gives a constant flux magnitude of $1.5 \cdot \hat{I} \cdot L$, previously represented by the dotted circle in Figure 2.4. In order to maintain a constant magnitude of the flux vector, the two remaining currents must be phase shifted, which is shown in Figure 2.6. The flux is reduced to $\cos(\pi/6)/1.5 = 1/\sqrt{3} \approx 0.58$ of the balanced case.

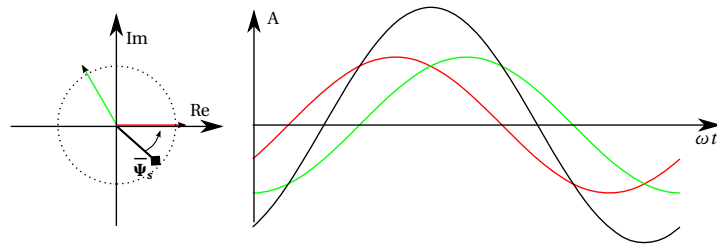


Figure 2.6: One phase lost, phase shift of 60 electrical degrees between the two remaining phase currents.

The black curve in Figure 2.6, represents the sum of I_a and I_b which is the current that must be conducted through the the fourth phase leg or the switch to the middle of the DC-link in Figure 2.3. The current from the star point is $2\hat{I}\cos(\pi/6) = \sqrt{3}$, as the angle between the two phase currents are 60 electrical degrees. As a consequence, it is therefore necessary to rate the fourth leg or the switch $\sqrt{3}$ times higher than the ordinary phase legs to be able to keep the same amplitude of the two remaining phase currents.

Chapter 3

Design of fault-tolerant fractional slot machines

Chapter 3 describes how the theory in Chapter 1 has been implemented when the fractional slot machines are designed. The chapter starts with an introduction of the design specification, that is based on the Toyota Prius Machine from 2004. A choice of pole/slot configurations is presented, while the final analysis of the designs are left to Chapter 4.

3.1 Design specification

The design specification has been chosen based on the physical dimensions of the Toyota Prius Machine from 2004, in order to design a fractional slot machine of similar physical size including the active parts. The Prius 2004 machine has been used as a reference as it has been investigated intensively and a lot of reference material is currently available. The end-windings are expected to be shorter for a fractional slot machine with concentrated windings compared to a machine with distributed windings. It has been assumed that the stator stack length can be extended by approximately 30%. In fact, the protrusion of the end-windings varies depending on many things; slot geometry, copper wires, manufacturing process etc. An interesting study, where the size of the end-windings are compared when the same stator is wound with; distributed windings, one-layer concentrated winding and two-layer concentrated winding is presented by [23]. More about estimation of the end-windings of the final designs can be found in Section 4.2.1. Some key parameters of the 2004 Prius are presented together with the design specification of the thesis design in Table 3.1.

Table 3.1: 2004 Prius [24] and Thesis design characteristics.

	Prius 2004	Thesis design
Outer stator diameter [mm]	269	269
Stator stack length [mm]	84	108 ¹
Rotor diameter [mm]	160.5	-
Cu [kg]	6.8	-
PM [kg]	1.232	-
Peak power [kW]	50	-
Peak torque [Nm]	400	-
Max speed [rpm]	6000	6000

3.1.1 Rating of the reference machine

The rating of an electric machine itself due to its own physical limitations, without taking inverter rating and the DC-link voltage etc. into account, are often determined by a thermal limit together with limitations of the mechanical structure and the electrical insulation. The different types of limitations are not independent as material properties varies with temperature and insulation material might be sensitive to both high temperatures and vibrations. If the electrical machine is used in a vehicle, it is likely that the machine is just one component among others that utilize the same cooling system. If that is the case, not even the thermal limit of the electric machine is a strictly independent property of the machine itself. Therefore, it is impossible to to make a meaningful comparison between two electric machines without introducing boundaries or restrictions.

In this thesis, the boundaries are based on the Toyota Prius 2004 "similar" drive system, which is tried to emulate the real drive system of the Toyota Prius 2004 as good as possible with the available data that is found. A model of the Prius 2004 machine following [25] (using the same geometry and material data) has been used and the result from the FEA is compared with the measurement results in [26]. It is worth mentioning, that tests that are presented in [27] show that the thermal limited continuous power ratings of the machine are approximately 21kW with 35° C coolant and 15kW with 105° C coolant, while the manufacturer specifies the continuous power rating of the machine to 30kW.

According to [26], a phase current of 250 A_{RMS} is needed to reach the specified peak-torque of 400Nm. The DC-link voltage can be boosted up to 500V. From that it follows that the maximum phase voltage is $500\sqrt{2}/\pi = 225V_{RMS}$ in three phase square wave modulation mode, which is a modulation technique that is

¹Based on the assumption that the expected shorter end-windings will allow for an increased active length of 30%.

used in the 2004 Prius drive system [26]. This means that the inverter must be rated at least to $3 \cdot 250 \cdot 225 = 169 \text{ kVA}$. The FEA result given for the kVA limitation is shown in Figure 3.1. The machine is operated at the MTPA point that fulfills the kVA limit at each speed. The output torque at 250 A_{RMS} from the FEA is 374 Nm which is about 6.5% lower than the reported torque for the same current. One can observe that the voltage limit is reached at about 2250 rpm, while the peak torque of the electrical machine is achieved up to 1200 rpm in the Prius 2004 drive system [26]. It is clear that the torque is limited before the voltage limit is reached, also discussed in [26].

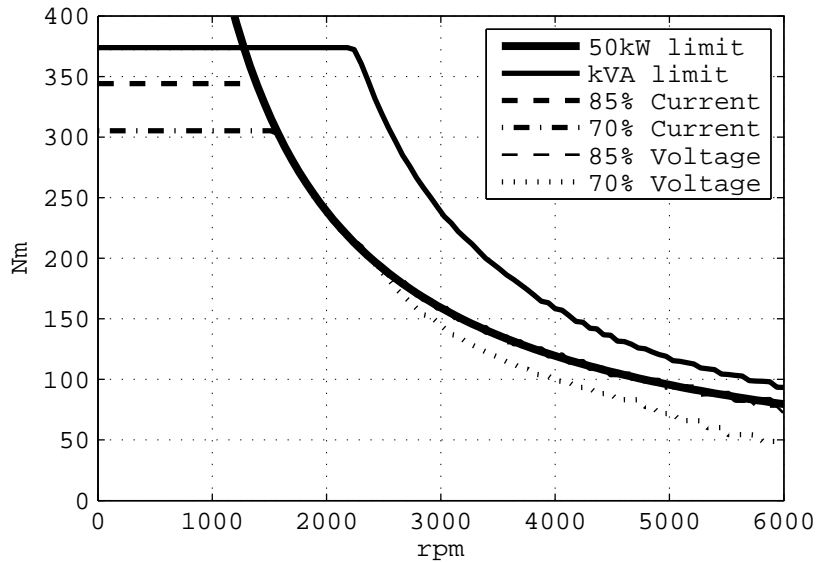


Figure 3.1: Torque speed characteristics of the Toyota Prius 2004 machine that is used as a reference.

Another limit is the supply of active power to the DC-link, which can be fed from the battery via the DC/DC-converter ($\approx 20 \text{ kW}$) and from the generator via the generator converter ($\approx 30 \text{ kW}$). In total, the active power is then limited to about 50 kW , which is also plotted in Figure 3.1. Considering the power limitation and the FEA torque, the peak torque is achieved up to 1270 rpm which is 5.8% higher than specified in [26]. The torque as function of speed is estimated based on approximate data provided by the Toyota Motor Company and presented in [26]. The overall picture is very similar to the power limit curve in Figure 3.1. According to [26], the torque at 6000 rpm is estimated to 60-70 Nm and the FEA model

shows about 75 Nm at the same speed.

In addition to the active power and kVA limit of the converter found, the sensitivity of the relatively high kVA limit was studied and presented in Figure 3.1. The voltage and current limits of the converter were reduced in two steps respectively (to 85% and to 70%). The effect of the current reduction (voltage at 100%) can be seen in the low speed region only, the torque is reduced and the speed limit of the peak torque is increased as a direct consequence of the power limit. The torque output is not affected when the current is put back to 100% and the voltage reduced to 85%, as the torque is still limited by the active power and not the voltage. If the voltage is reduced to 70%, the torque is voltage limited from approximately 2500 rpm, while it is power limited in the range 1270-2500 rpm and current limited in the range 0-1270 rpm.

It should be noted that a set of i_d and i_q combinations exists for each speed and torque level, where the shortest current vector corresponds to the MTPA operating point. When the voltage was reduced to 85%, it is still possible that a subset of i_d and i_q combinations including the original MTPA operating point is disqualified due to voltage limitation and a new MTPA operating point that fulfills the voltage limitation is found. This can not be seen in the torque speed diagram in Figure 3.1, as the same torque level is maintained. This is an interesting aspect when it comes to turn selections of the machines. It might be possible to choose a high number of turns without limitation of the torque at higher speeds as it is limited by active power rather than voltage. On the other hand, it is possible that a higher number of turns will result in an increased transfer of reactive power between the converter and the machine as the power factor is affected.

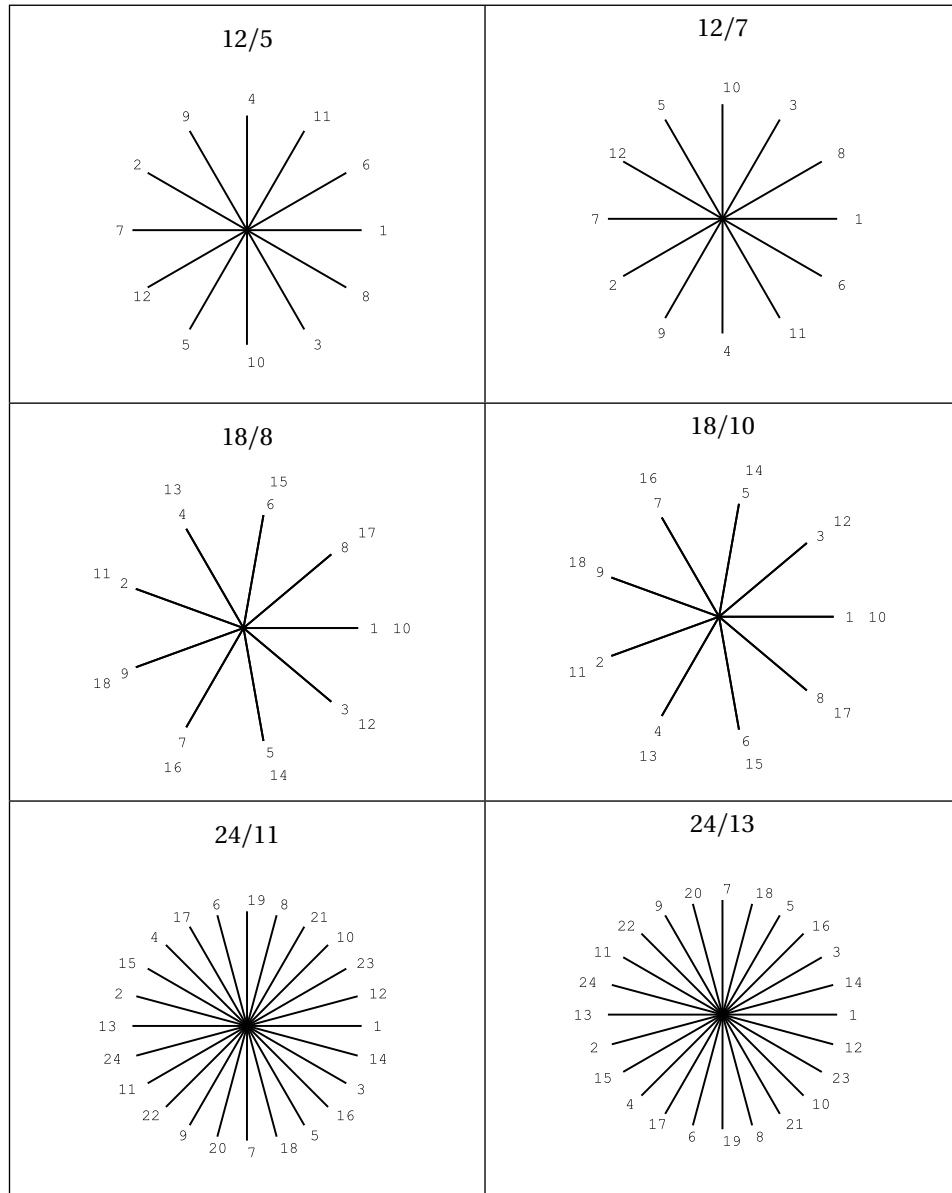
3.2 Selection of pole and slot combination

Some feasible pole and slot combinations were previously shown in Table 1.1, where both $Q_s = 2p \pm 1$ and $Q_s = 2p \pm 2$ combinations were presented. The $Q_s = 2p \pm 1$ combinations result in an odd number of slots and teeth per phase which is not regarded as a suitable choice for a fault tolerant machine, as the sum of the induced flux per phase cannot be zero. For all the $Q_s = 2p \pm 1$ combinations, the flux from one phase must link to another phase and it will result in a considerable mutual inductance between the phases.

Remaining are the $Q_s = 2p \pm 2$ combinations, which result in an even number of teeth per phase and possibly a very low mutual coupling between phases depending on the winding configuration. Back-EMF phasor diagrams for $Q_s = 2p \pm 2$ combinations from $p = 5$ to $p = 13$ are shown in Table 3.2. It can be seen that machines with the same number of slots, Q_s , will result in the same winding

configuration as the phasor diagrams are just mirrored.

Table 3.2: Back-EMF phasor diagrams.



Models of the resulting three stator configurations that might be of interest are

created in FEA models and are shown in Figure 3.2. No permanent magnets are introduced, the rotors are just solid iron cores, and the stators are excited according to their respective winding configuration. The grey or shadowed areas represents the teeth of one phase in each stator configuration. It can be seen that groups of an even number of teeth, 2 and 4, appear for the 12/5 and 24/11 configurations while the 18/8 configuration shows groups of an odd number, 3. One can conclude that the phases of the 18/8 configuration are harder magnetically coupled than for the other two configurations. The local sum of the flux from an odd group of teeth cannot be zero, thus more flux lines from the grey teeth link the neighboring teeth, see Figure 3.2. Therefore, only the $Q_s = 12$ and $Q_s = 24$ are finally regarded as interesting choices.

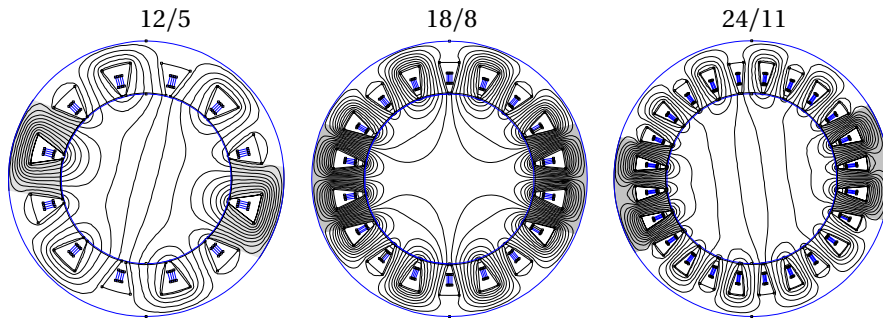


Figure 3.2: Flux lines representing induced flux for three different pole slot combinations.

Another interesting aspect when studying Figure 3.2, is that the lowest possible MMF subharmonic with a wave length that equals 2π mechanical rad can be seen. It causes the flux lines that crosses straight through the rotor and is present in the $Q_s = 12$ and $Q_s = 24$ but not in the $Q_s = 18$ stator configuration.

The MMF harmonics of the 12/5 and 12/7 configurations have already been used as an example in section 1.7 and are presented in Figure 1.9. It is clear that the 12/5 arrangement provides a more advantageous MMF harmonics pattern in relation to the fundamental. The two pole configurations are compared when used in an axial flux machine configuration in [28]. In that case the rotor losses for the $p = 7$ is about twice compared to the $p = 5$. Their winding factors are the same and $p = 5$ is therefore considered for the $Q_s = 12$ configuration.

When it comes to the 24/11 and 24/13 configurations, it can be seen in Figure 3.3 that the 24/11 arrangements gives a somewhat lower harmonic content in the MMF wave.

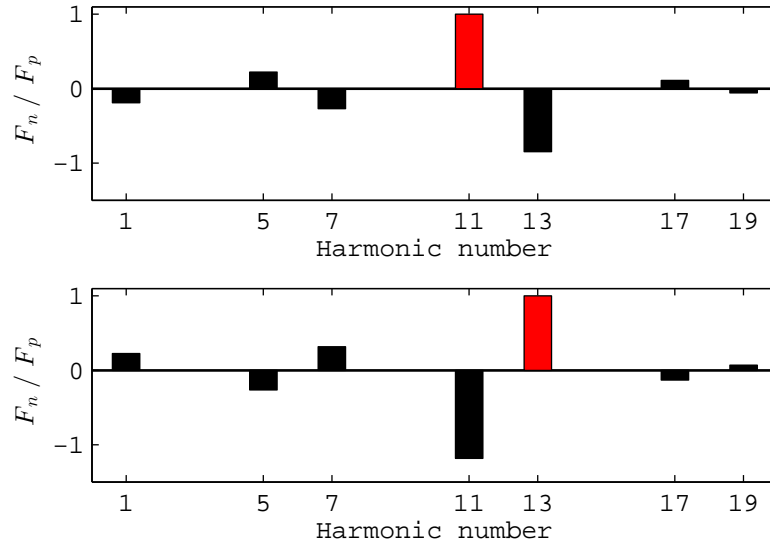


Figure 3.3: Harmonic content in the air-gap for the $p = 11$ and $p = 13$ machine respectively. The amplitudes are related to the fundamentals which corresponds to the red bars.

The relative frequency of the MMF harmonics on the rotor side are shown in Figure 3.4. It can be seen that the relative frequency of the fundamental component is zero in both configurations and that the relative frequency of the 5th and 7th harmonics is shifted somehow, in a similar way as the 17th and 19th. As the winding factors are the same for both pole numbers but the pole numbers are relatively high, the $p = 11$ is considered for the $Q_s = 24$ configuration.

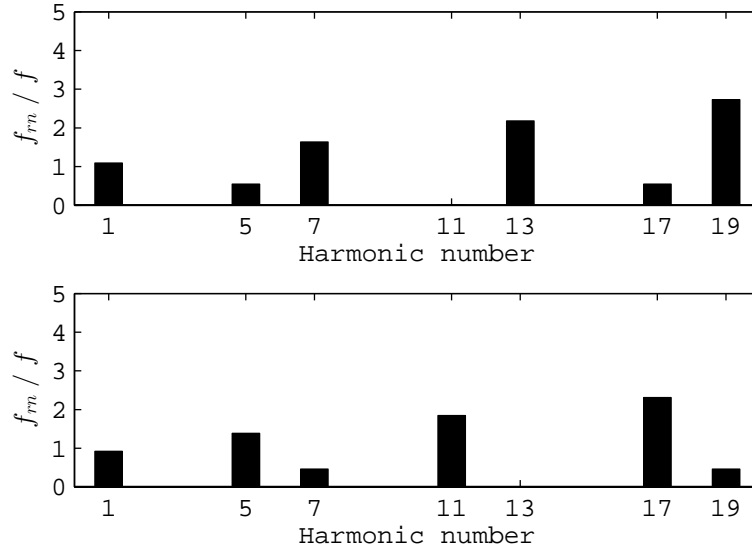


Figure 3.4: Relative frequency of the MMF harmonics on the rotor side. The frequency of the fundamental $n = p = 11$ and $n = p = 13$ equals zero for both configurations.

It is difficult to motivate a choice of just one of the remaining configurations. One could argue that the number of poles $p = 11$ is too high and thereby limit the electrical/mechanical frequency and as a consequence also the output power. On the other hand, the 24/11 offers both lower MMF harmonic content and a slightly higher winding factor. Lowered MMF harmonic content is expected to reduce the rotor and PM losses. If the frequency of the 12/5 configuration is limited by the losses caused by MMF wave harmonics rather than the frequency of the fundamental, the 24/11 might be a better choice. Another aspect is that the stator yoke becomes rather bulky when the rotor diameter, hence the total magnetic flux from a permanent magnet, is increased later shown in (3.3) in Section 3.4.3. It is therefore possible that a higher pole number suits the decided design specification better. In the end, it is the combined weight of torque and speed characteristics of the two machines that can motivate a final choice. The 24/11 is expected to give a higher torque output than the 12/5 at lower frequencies, but it is not obvious that the 12/5 can operate at higher frequencies than the 24/11 due to the complex nature of the losses caused by the MMF harmonics.

3.3 FEA and material data

This section presents how the FEA has been carried out through the thesis work and also the data that have been used.

3.3.1 Finite Element Analysis

The electromagnetic part of the finite element analysis has been carried out in ANSYS Maxwell v.15, while the thermal part of the finite element analysis has been carried out in femm 4.2. Except for Figure 3.2 that is produced for illustrative purpose only, in femm 4.2. All models are created based on 2D geometries, where the electromagnetic part is carried out in static as well as in transient modeling mode. The thermal modeling is made only in static mode and rather simplified models has been used.

3.3.2 Material data

Copper

In the FEA, the current is modeled to be uniform through the 2D winding object. The current density in the winding object has been scaled according to the fill-factor and the slot area. The fill-factor is defined as the ratio between the total cross-sectional area of the copper that occupies the slot area and the slot area itself, the insulation is not included. The definition that has been used for slot area, A_{slot} , can be seen in Figure 3.5. A copper fill-factor of 0.5 has been assumed for all the fractional slot machine designs. The electric copper resistivity is put to $2.39 \cdot 10^{-8} \Omega m$ corresponding to a temperature of $120^\circ C$. The thermal conductivity of copper has been put to $400 W/(m \cdot K)$ but an equivalent thermal conductivity for copper and impregnation material, called winding mix, are used when modeling slots. The thermal conductivity of the winding mix has been varied and the values that are used are presented together with the results.

Iron

A non-linear model of the lamination material as presented in [25], have been used for all the machine designs. A thermal conductivity of $28 W/(m \cdot K)$ has been used along the lamination sheets.

Permanent magnets

A model based on the residual flux density, B_r , the relative permeability, μ_r , and the electric conductivity, σ , of the PMs has been used in the FEA. Data for two different permanent magnets, PM1 and PM2, are specified in Table 3.3. PM2 is used in the FEA of the Prius 2004 reference machine and the data are given in

[25]. PM1 was chosen for the thesis designs due to its lower electric conductivity and the expected eddy current loss in the PMs of a fractional slot machine. There are actually several PM material with the lower conductivity and similar characteristics available at [29], but the choice was made to reflect N30AHZ due to its high maximum recommended working temperature of $220^{\circ}C$.

Table 3.3: Material properties of the two different permanent magnet materials that are used.

Parameter	PM1	PM2
$B_r[T]$	1.1	1.19
μ_r	1.04	1.03
$\sigma[S/m]$	$5.56 \cdot 10^5$	$6.25 \cdot 10^5$

3.4 Design strategy

The design strategy is to vary a number of parameters for both the selected configurations, $Q_s=12/p=5$ and $Q_s=24/p=11$. Then, to use FEA to evaluate the designs and to find the most promising candidates of each configuration, within the interval of the chosen parameters. About ten variables here called "geometry parameters", excluding information about the windings, are needed to geometrically define the machine designs and they are presented in Section 3.4.3. Instead of just sweeping all the geometry variables, four "design variables" were defined. The aim of introducing the four design variables is to reduce the number of design combinations and thereby limit the computational time, but also to use a limited set of variables that hopefully make more sense to the human mind when evaluating the result.

3.4.1 Design variables

In this section a short explanation follows of the ideas behind the four design variables. The ranges within each design variable, are also presented.

Rotor diameter, D_r

The rotor diameter is considered as one of the most important variables. For a fixed active length, it determines the cross-sectional area of the air-gap as well as at which radius the air-gap is located. Both these properties of the air-gap are extremely important for the torque production which takes place in the air-gap. For a fixed outer stator diameter, it defines also the ratio between the stator and the rotor volume. From that perspective, it determines also the possible proportions between electric and magnetic loading for a PMSM to some extent.

The rotor diameter is chosen to be varied in 10 mm steps between 150 mm and 200 mm.

Air-gap length, l_g

Another important variable is the air-gap length, which determines the magnetic coupling between the stator and the rotor. A shorter air-gap length lowers the reluctance of the gap and increases the flux for a fixed permanent magnet length or induced MMF-wave. This may imply that the amount of permanent magnets and copper can be reduced. On the other hand, apart from possible mechanical issues associated with narrow air-gaps, it gives also a more non-linear machine. The total reluctance of the magnetic circuit will be more sensitive to the non-linear reluctance of the iron path, which is relatively more significant when compared to a low air-gap reluctance. Air-gap lengths of 0.8 mm and 1.2 mm have been used.

Stator flux density, B_{max}

The flux density level is an important aspect, why a stator flux density variable, B_{max} , is defined. B_{max} is the maximal average permanent magnet flux density over the cross-sectional area along a flux path. The aim is to design a stator structure with a constant flux density along the flux path following the philosophy presented in Section 1.3. Parts where the flux path is well defined, such as the yoke, can be calculated easily while parts where the flux path is not well defined, such as the shoe of the teeth, is not that straightforward. One lighter and one heavier stator structure is designed, corresponding to stator flux levels of 1.5 T and 1.3 T respectively. As two flux levels for the same magnetic loading is used, the combination of PM and induced flux is altered which was discussed in Section 1.1.

Air-gap flux density, \hat{B}_1

Air-gap flux density, \hat{B}_1 , corresponds directly to the magnetic loading and is not expected to require any further explanation. Peak flux densities of 0.85 T and 1 T are used.

3.4.2 Design variable combinations

The sets of the design variables presented in the previous section result in 48 different combinations. Each combination result in a machine design that is labeled with a number and collected in Table 3.4.

Table 3.4: Design variable combinations and their motor index.

#	D_r	l_g	B_{max}	\hat{B}_1	#	D_r	l_g	B_{max}	\hat{B}_1
1	150	0.8	1.3	0.85	25	180	0.8	1.3	0.85
2	150	0.8	1.3	1	26	180	0.8	1.3	1
3	150	0.8	1.5	0.85	27	180	0.8	1.5	0.85
4	150	0.8	1.5	1	28	180	0.8	1.5	1
5	150	1.2	1.3	0.85	29	180	1.2	1.3	0.85
6	150	1.2	1.3	1	30	180	1.2	1.3	1
7	150	1.2	1.5	0.85	31	180	1.2	1.5	0.85
8	150	1.2	1.5	1	32	180	1.2	1.5	1
9	160	0.8	1.3	0.85	33	190	0.8	1.3	0.85
10	160	0.8	1.3	1	34	190	0.8	1.3	1
11	160	0.8	1.5	0.85	35	190	0.8	1.5	0.85
12	160	0.8	1.5	1	36	190	0.8	1.5	1
13	160	1.2	1.3	0.85	37	190	1.2	1.3	0.85
14	160	1.2	1.3	1	38	190	1.2	1.3	1
15	160	1.2	1.5	0.85	39	190	1.2	1.5	0.85
16	160	1.2	1.5	1	40	190	1.2	1.5	1
17	170	0.8	1.3	0.85	41	200	0.8	1.3	0.85
18	170	0.8	1.3	1	42	200	0.8	1.3	1
19	170	0.8	1.5	0.85	43	200	0.8	1.5	0.85
20	170	0.8	1.5	1	44	200	0.8	1.5	1
21	170	1.2	1.3	0.85	45	200	1.2	1.3	0.85
22	170	1.2	1.3	1	46	200	1.2	1.3	1
23	170	1.2	1.5	0.85	47	200	1.2	1.5	0.85
24	170	1.2	1.5	1	48	200	1.2	1.5	1

3.4.3 From design variables to geometry parameters

Besides the rotor diameter, D_r , and the outer stator diameter, D_{out} , eight more parameters are needed to define the complete 2D machine geometry, see Figure 3.5. Six of the parameters are calculated and updated for each design variable configuration while five are held fixed.

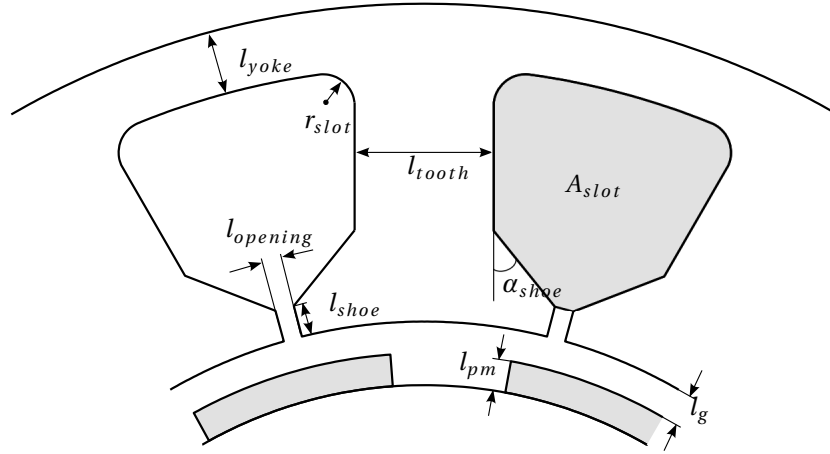


Figure 3.5: The eight geometry parameters that together with the rotor diameter, D_r , and the outer stator diameter, D_{out} , define the 2D machine geometry. The grey area in the right hand slot defines the slot area, A_{slot} , that is used when the fill-factor is calculated.

Permanent magnet length

The permanent magnet length, l_{pm} , is calculated based on the air-gap length, l_g , and the desired air-gap flux density, \hat{B}_1 , using (1.4) and (1.5) in Section 1.2. The calculated permanent magnet lengths that are required for the four combinations of l_g and \hat{B}_1 are shown in Table 3.5.

Table 3.5: Required permanent magnet length, l_{pm} , in mm.

		Air gap length, l_g [mm]	
		0.8	1.2
\hat{B}_1 [T]	0.85	1.9	2.8
	1	3.8	5.6

The permanent magnet length is varied within a great interval, it is likely that the shortest permanent magnet length of 1.9 mm will cause manufacturing issues. This has not been investigated further since it is not used in the final designs.

Stator yoke and teeth

The total flux from a permanent magnet can be calculated approximately by integrating the square shaped flux, B_m , in Figure 1.3. For a permanent magnet

that covers 2/3 of a pole pitch it becomes

$$\phi_m = B_m \frac{\pi(D_r + 2l_{pm})2/3}{2p} \quad (3.1)$$

which is the maximum magnetic flux that links a tooth. The required thickness of the tooth, l_{tooth} , for a given stator flux density, B_{max} , is then calculated according to

$$l_{tooth} = \frac{\phi_m}{B_{max}} \quad (3.2)$$

When the PM flux that links a tooth enter the yoke region it divides about equal between the two paths that links the two neighboring teeth. Hence, the required thickness of the stator yoke for the same flux density is calculated as

$$l_{yoke} = \frac{\phi_m}{2B_{max}} \quad (3.3)$$

Fixed parameters

The fixed parameters and the values used can be seen in Table 3.6. The assumed values used for the parameters that have been held fixed is based on discussions and what is commonly used in existing machines. Values are therefore open for modifications if the machines are to be prototyped.

Table 3.6: Geometry parameters that are not affected by the design variables and held fixed.

Parameter	value
D_{out}	269 mm
r_{slot}	5 mm
l_{shoe}	2 mm
α_{shoe}	45°
$l_{opening}$	3 mm

Chapter 4

Analysis of fault-tolerant fractional slot machine designs

In this chapter, the 48 design variable combinations of each pole/slot combination are evaluated in order to motivate a choice from each set of combinations. An appropriate number of turns are selected for the windings of the machines and the impact of phase current on winding temperature rise is analyzed. The two final machine designs are compared together with the Toyota Prius from 2004 in terms of performance and material cost. Some key figures from the comparison of the three machines are summarized in the end of this chapter.

4.1 Machine design selection

The 48 machines are evaluated by comparing their torque production in relation to the material cost, [Nm/USD]. The material market price have fluctuated substantially over the last years, especially for neodymium which today is back on the same price levels as in 2010 (≈ 100 USD/kg) from the peak during 2011 (≈ 500 USD/kg). Due to the variation of the material cost, the current material cost is estimated and the results are presented to take cost variation of each material into account.

4.1.1 Estimation of the current material costs

Accurate calculations of the material costs is a difficult or even impossible task, since the material prices varies substantially over time as mentioned previously. Also the price at two different markets may not be the same at the same time.

The estimations presented in this section are based on information collected in the beginning of August in 2014. The current material cost estimation is presented in Table 4.1.

Table 4.1: Current material cost estimation.

Material	Cost [USD/kg]	Cost [SEK/kg]
Copper	7.1	49
Iron	2.1	14.4
PM	82.3	566

Copper

The material cost of copper that is used in this thesis, is an average of the three month average prices at London Metal Exchange (LME) and Commodity Exchange (COMEX) respectively.

Table 4.2: Three month average copper price presented at [30].

3 Month average price [USD/kg]	
LME	7.0960
COMEX	7.1650
Average	7.1

Iron

The material cost of the iron varies depending on the alloy content. Silicone steel had been rather stable at around 2.1 USD/kg the last three month, when data was collected in August 2014 [31].

Permanent magnets

Typical rare earth element content in neodymium magnets together with the chinese export prices are shown in Table 4.3. The values of the typical element content are 2-3 years old and it is possible that they are slightly lower today. There is at least an incentive to strive to lower them due to their relatively high price. The metal prices presented at [31] have been recalculated manually to a corresponding three month average.

Table 4.3: Rare earth element content in Neodymium magnets together with the chinese export prices.

Element	Typical weight	USD/kg
Neodymium	31% [32]	92.5 [31]
Dysprosium	8.5-11% [33]	550 [31]
Magnet	31% and 9.75 %	82.3

4.1.2 Torque per cost for different cost scenarios

It was concluded at an early stage that the Prius 2004 reference machine offers a quite high peak torque, why it was natural to sort out promising designs based on torque production. An aspect on torque production is that basically any PMSM produces higher torque if more permanent magnets are added to the rotor or if the machine is made larger. When the physical size or volume of the machine is used as a boundary for the design, an increase of one material or part will automatically lead to a decrease of another material or part. An important aspect is the balance between materials and parts, one want to know if it is more effective to add 100g of PM material to increase the magnetic loading than adding 100g of copper to increase the electric loading. Maybe even more interesting to see if 2 USD of PM material pays back better than 2 USD of copper in terms of machine performance.

Cost scenario diagrams were introduced in order to visualize the comparison of the performance to cost ratio for different machine designs. In this thesis, the ratios between torque production and material cost are compared. One can imagine a scenario where the PM material cost is very high and it is therefore beneficial to minimize the use of PM material. In another scenario, the PM material cost may have been reduced significantly and it is therefore beneficial to increase the use of PM material.

Cost scenario diagrams

An example of a cost scenario diagram is shown in Figure 4.1; permanent magnet cost on the vertical axis and copper cost on the horizontal axis. Point A is the default cost relation (Fe:Cu:PM), given by (2.1:7.1:82.3)=(1:3.4:39), previously presented in Table 4.1. Point B corresponds to a default iron price while both the copper and PM prices are increased by 50%, or a situation where the copper and PM prices keep their initial values while the iron price is reduced by 33%. In this way, the effect of a varying iron price can also be considered. Finally, point C refer to default iron and PM prices but a copper price that is reduced by 50%.

In order to make cost scenario diagrams, the torque production per cost is calculated for all the machines and different material cost scenarios according to

$$x_n = \frac{T_n}{m_{Fe}\$_{Fe} + m_{Cu}\$_{Cu} + m_{PM}\$_{PM}} \quad (4.1)$$

where m represents the mass of each material to produce the respective machine, n , and $\$$ is the material cost of each material. The maximum torque production per cost, $max(x_n)$, is calculated for each cost scenario. Machines that produce 95% or more torque per cost in comparison with the best machine is considered as competitive designs for the cost scenario. All competitive machines, $x_n \geq max(x_n) \cdot 0.95$, are rewarded with a black dot in their cost scenario diagram.

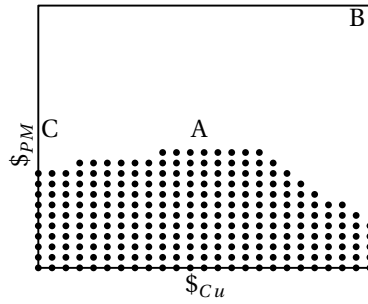


Figure 4.1: Example of a cost scenario diagram.

Regarding the example in Figure 4.1, the here investigated machine is not considered as a competitive machine design given the current material cost scenario, as there is no dot at point A. It is considered as competitive if the price of the permanent magnets is slightly reduced, as there are dots in the lower part of the diagram. It can also be seen that this particular design is not that sensitive to the price of copper when compared to the other designs.

4.1.3 Cost efficiency of the 12/5 machine designs

The output torque has been calculated at a speed of 1500 rpm for five different excitation levels, $J = [5 \ 10 \ 15 \ 20] \text{ A/mm}^2$, in the direction of the quadrature axis ($i_d = 0$). This to see the non-linear behavior of the machines and not to compare them in just one operating point.

The cost scenario diagrams for the 48 machine designs, previously presented in Table 3.4, excited by 5 A/mm^2 are shown in Table 4.4. It can be seen that the most cost competitive machines have a rotor diameter of 150-160 mm, and an air-gap of 0.8 mm. The maximal average permanent magnet flux density level, B_{max} , is not that critical at this relatively low current levels. It is clear that an air-gap flux density, \hat{B}_1 , of 1 T is preferable compared to 0.85 T. Machine 2, 4 and 12 are the most cost competitive at the estimated current material cost scenario.

Table 4.4: Cost scenario diagram for the 48 $Q_s=12/p=5$ machine designs at an excitation level of 5 A/mm^2 .

		$l_g = 0.8$				$l_g = 1.2$			
		\hat{B}_1							
		0.85	1	0.85	1	0.85	1	0.85	1
D_r	150	1	2	3	4	5	6	7	8
	160	9	10	11	12	13	14	15	16
	170	17	18	19	20	21	22	23	24
	180	25	26	27	28	29	30	31	32
	190	33	34	35	36	37	38	39	40
	200	41	42	43	44	45	46	47	48
		1.3		1.5		1.3		1.5	
		B_{max}							

Table 4.5 shows cost scenario diagrams when the current excitation is $10 A/mm^2$, twice as high as in the previous case. In this case, a maximal average permanent magnet flux density level of 1.3 T is clearly preferable compared to 1.5 T. It can be seen that machine number 6 is competitive at this excitation level if the price of permanent magnets are reduced. One can also observe a shift towards greater rotor diameters.

Table 4.5: Cost scenario diagram for the 48 $Q_s=12/p=5$ machine designs at an excitation level of $10 A/mm^2$.

		$I_g = 0.8$				$I_g = 1.2$			
		B_1							
		0.85	1	0.85	1	0.85	1	0.85	1
D_r	150	1	2	3	4	5	6	7	8
	160	9	10	11	12	13	14	15	16
	170	17	18	19	20	21	22	23	24
	180	25	26	27	28	29	30	31	32
	190	33	34	35	36	37	38	39	40
	200	41	42	43	44	45	46	47	48
		1.3		1.5		1.3		1.5	
		B_{max}							

When increasing the current density $5A/mm^2$ further, the same but magnified tendencies are shown as before. The design variables of the air-gap and stator flux densities are at the same level for all the competitive machines. An air-gap length of 1.2 mm is still not beneficial considering the current cost scenario, but it will be by machine number 6 and 14 if the PM cost is lowered slightly.

Table 4.6: Cost scenario diagram for the 48 $Q_s=12/p=5$ machine designs at an excitation level of $15 A/mm^2$.

		$l_g = 0.8$				$l_g = 1.2$			
		\hat{B}_1							
		0.85	1	0.85	1	0.85	1	0.85	1
D_r	150	1	2	3	4	5	6	7	8
	160	9	10	11	12	13	14	15	16
	170	17	18	19	20	21	22	23	24
	180	25	26	27	28	29	30	31	32
	190	33	34	35	36	37	38	39	40
	200	41	42	43	44	45	46	47	48
		1.3		1.5		1.3		1.5	
		B_{max}							

As a last step, the current density is increased up to $20 A/mm^2$, and the result is shown in Table 4.7. It can be seen that there is one machine design, number 14, that benefits from an increased air-gap length of, $l_g = 1.2$ mm, at this relatively high excitation level.

Table 4.7: Cost scenario diagram for the 48 $Q_s=12/p=5$ machine designs at an excitation level of $20 A/mm^2$.

		$l_g = 0.8$				$l_g = 1.2$			
		\hat{B}_1							
		0.85	1	0.85	1	0.85	1	0.85	1
D_r	150	1	2	3	4	5	6	7	8
	160	9	10	11	12	13	14	15	16
	170	17	18	19	20	21	22	23	24
	180	25	26	27	28	29	30	31	32
	190	33	34	35	36	37	38	39	40
	200	41	42	43	44	45	46	47	48
		1.3		1.5		1.3		1.5	
		B_{max}							

Based on the overall cost efficiency, considering all the four excitations levels, machine design number 10 turned out to be a favorable choice. Machine number 10 is therefore highlighted when the 12/5 machine designs are evaluated further.

4.1.4 Cost efficiency of the 24/11 machine designs

The cost scenario diagrams for the $Q_s=24/p=11$ machine designs have been calculated in exactly the same manner as in the previous section. The 48 designs, excited by $5 A/mm^2$ are shown in Table 4.8. It can be seen that more machines turned out to be cost effective if comparing with the same excitation level for the $Q_s=12/p=5$ machine designs in Table 4.4. There are also several machines with lower air-gap flux density, $\hat{B}_1=0.85$ T, that are competitive at this relatively low current level. It can also be seen that there is a general shift towards higher rotor diameters compared with the $Q_s=12/p=5$ machine designs. This can be explained by the thinner stator diameter that is required when the number of poles are increased.

Table 4.8: Cost scenario diagram for the 48 $Q_s=24/p=11$ machine designs at an excitation level of $5 A/mm^2$.

		$l_g = 0.8$				$l_g = 1.2$			
		\hat{B}_1							
		0.85	1	0.85	1	0.85	1	0.85	1
D_r	150	1	2	3	4	5	6	7	8
	160	9	10	11	12	13	14	15	16
	170	17	18	19	20	21	22	23	24
	180	25	26	27	28	29	30	31	32
	190	33	34	35	36	37	38	39	40
	200	41	42	43	44	45	46	47	48
		1.3		1.5		1.3		1.5	
		B_{max}							

When increasing the current density to 10 A/mm^2 , as shown in Table 4.9, there is a further shift towards higher rotor diameters but also a shift towards higher air-gap flux densities. At the current cost scenario, only machine design number 28 is competitive on the higher stator flux density level of $B_{max}=1.5 \text{ T}$.

Table 4.9: Cost scenario diagram for the 48 $Q_s=24/p=11$ machine designs at an excitation level of 10 A/mm^2 .

		$I_g = 0.8$				$I_g = 1.2$			
		\hat{B}_1							
		0.85	1	0.85	1	0.85	1	0.85	1
D_r	150	1	2	3	4	5	6	7	8
	160	9	10	11	12	13	14	15	16
	170	17	18	19	20	21	22	23	24
	180	25	26	27	28	29	30	31	32
	190	33	34	35	36	37	38	39	40
	200	41	42	43	44	45	46	47	48
		1.3		1.5		1.3		1.5	
		B_{max}							

Cost scenario diagrams for a current excitation level of $15 A/mm^2$ are shown in Table 4.10. The previous trend towards higher rotor diameters and air-gap flux density continues.

Table 4.10: Cost scenario diagram for the 48 $Q_s=24/p=11$ machine designs at an excitation level of $15 A/mm^2$.

		$l_g = 0.8$				$l_g = 1.2$			
		\hat{B}_1							
		0.85	1	0.85	1	0.85	1	0.85	1
D_r	150	1	2	3	4	5	6	7	8
	160	9	10	11	12	13	14	15	16
	170	17	18	19	20	21	22	23	24
	180	25	26	27	28	29	30	31	32
	190	33	34	35	36	37	38	39	40
	200	41	42	43	44	45	46	47	48
		1.3		1.5		1.3		1.5	
		B_{max}							

The cost scenario diagrams for the highest excitation level, $20 A/mm^2$, of the $Q_s = 24/p = 11$ machine design are presented in Table 4.11. It can be seen that there are only two designs that are competitive at the current cost scenario, number 26 and 34. Both machines have the same design variables except for the rotor diameter.

Table 4.11: Cost scenario diagram for the 48 $Q_s=24/p=11$ machine designs at an excitation level of $20 A/mm^2$.

		$l_g = 0.8$				$l_g = 1.2$			
		\hat{B}_1							
		0.85	1	0.85	1	0.85	1	0.85	1
D_r	150	1	2	3	4	5	6	7	8
	160	9	10	11	12	13	14	15	16
	170	17	18	19	20	21	22	23	24
	180	25	26	27	28	29	30	31	32
	190	33	34	35	36	37	38	39	40
	200	41	42	43	44	45	46	47	48
		1.3		1.5		1.3		1.5	
		B_{max}							

It can be noticed that none of the designs where the air-gap length, $l_g=1.2$ mm, are cost competitive for the $Q_s=24/p=11$ designs. However, it can be mentioned that when studying the output torque at the highest current density of $20A/mm^2$, regardless of the machine cost; it was actually the machines with an air-gap length of, $l_g=1.2$ mm, that delivered the highest torque for both the $Q_s=12/p=5$ and the $Q_s=24/p=11$ designs. The higher torque is produced to an considerably increase of the PM cost, as the PM lengths are increased according to Table 3.5, why it can't be seen in the cost scenario diagrams.

Both machine number 18 and 26 turned out to be cost efficient when considering all the four excitation levels. Except for the highest excitation level, machine

18 is favorable while machine number 26 is favorable with exception from the lowest excitation. Both machine number 18 and 26 are therefore highlighted when the 24/11 configurations are evaluated further.

4.1.5 Torque speed characteristics of the 12/5 machine designs

The torque speed characteristics are calculated based on the 10 A/mm^2 operating point from the cost scenario section. Appropriate turn selections are calculated for each machine design in order to enter field weakening as close as possible to 2250 rpm, as the number of turns must be chosen as a discrete value. The turn selections are made for an excitation of 10 A/mm^2 and a maximum peak phase voltage of $V_{ph-max} = 500 \cdot 2/\pi \text{ V}$.

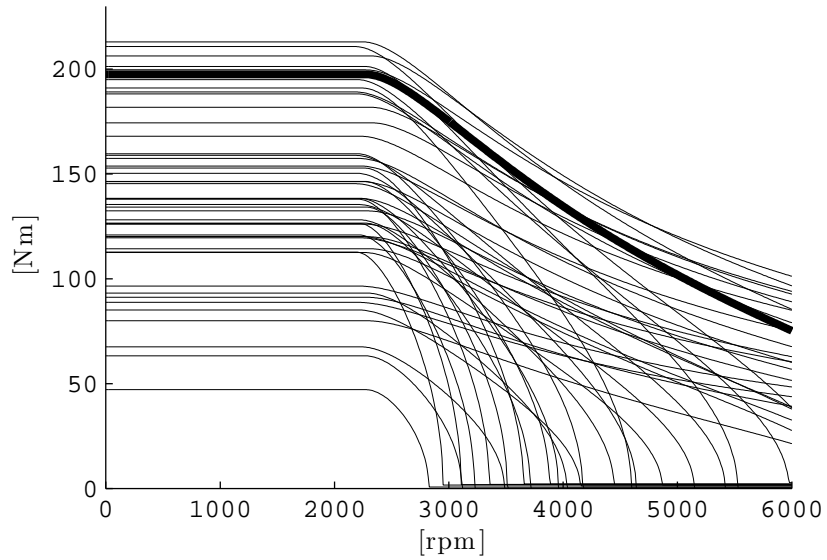


Figure 4.2: Torque speed characteristics for the 48 design combinations when $n_n = 2250 \text{ rpm}$, 10 A/mm^2 and $V_{ph-max} = 500 \cdot 2/\pi \text{ V}$. Machine number 10 is plotted using a thicker line width.

The torque speed characteristics of the 48 design combinations of the $Q_s=12/p=5$ configuration are shown in Figure 4.2. Machine number 10 was regarded as the most promising design considering the evaluation of the cost scenario diagrams previously, machine number 10 is therefore plotted using a thicker line width in Figure 4.2. It can be seen that machine number 10 is not only cost effective, it

offers also a reasonable torque speed characteristics compared to its competitors. Machine number 10 is therefore chosen as the final $Q_s=12/p=5$ design and called **machine A** from now and on.

4.1.6 Torque speed characteristics of the 24/11 machine designs

Figure 4.3 shows the torque speed characteristics of all the 48 design combinations for the $Q_s=24/p=11$ configuration, calculated in the same way as in the previous section. Both machine number 18 and number 26 were regarded as promising designs when evaluating the cost diagrams. The two most interesting designs are plotted using thicker lines in Figure 4.3. Both the machines offers approximately the same peak torque when excited by $10 A/mm^2$ but machine 26 shows a better torque speed performance in the field weakening region. Machine number 26 is therefore chosen as the final $Q_s=24/p=11$ design and called **machine B** from now and on.

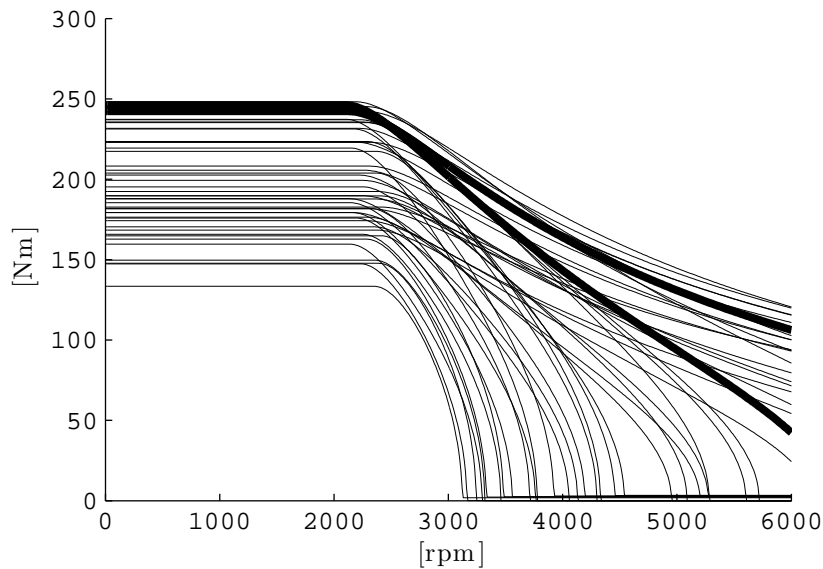


Figure 4.3: Torque speed characteristics for the 48 design combinations when $n_n = 2250$ rpm, $10 A/mm^2$ and $V_{ph-max} = 500 \cdot 2/\pi$ V. Machine number 18 and 26 are plotted using a thicker line width.

4.2 The two selected machine designs

The geometry of machine A and B are shown in Figure 4.4.

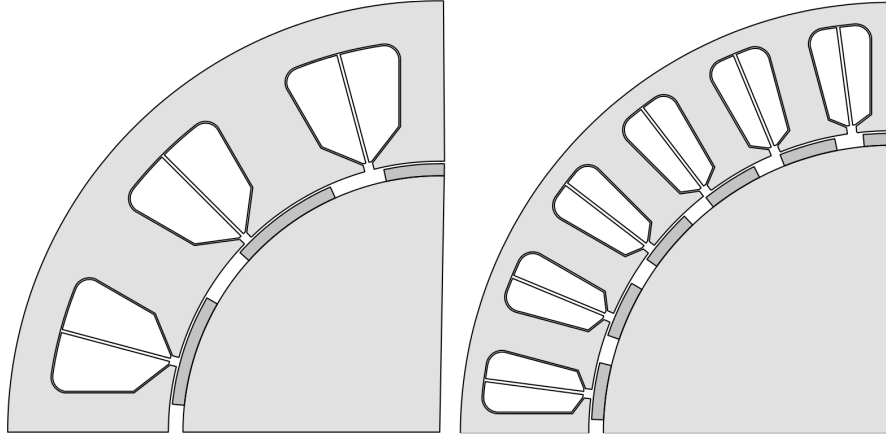


Figure 4.4: Geometry of machine A and machine B

4.2.1 Estimation of end-windings

The protrusion of the end-windings has been estimated according to the illustration in Figure 4.5, where the width of the coil, W_{cu} , is calculated as half the average slot width. The average slot width has been estimated as

$$W_{cu} = \frac{\pi(D_r/2 + l_{pm} + l_g + l_{shoe} + D_{out} - l_{yoke}) - Q_s l_{tooth}}{2Q_s} \quad (4.2)$$

The bend of the coil is assumed to have a minimum bend radius, r_{cu} . The total space occupied by the end-windings in axial direction is then $2(W_{cu} + r_{cu})$. The calculated values for the two machines are presented in Table 4.12.

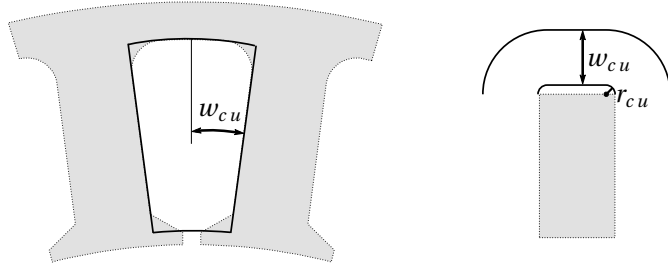


Figure 4.5: Illustration of how the axial protrusion of the end-windings have been estimated.

No measured values of the total length (stator stack + end-windings) of the Prius 2004 machine was found. However, using the known stack length of 84 mm and a photograph presented in [34], the total length was estimated to be around 140 mm. According to [35], the end-windings or the "coil-end length" of the Toyota Prius 2010 machine are 29 mm each. In [24] it is shown that the winding configuration of the 2004 and the 2010 Prius machines are not identical but similar. The total length of the 2004 Prius stack length in [24] and the end-windings of the 2010 Prius in [35] is 142 mm.

If a total length of 140 mm is assumed together with the values presented in Table 4.12, it was possible to extend the 2004 Prius stack length by 24% for machine A and by 40% for machine B. These numbers are to be compared with the assumption of 30% made in section 3.1. By adding the estimated end-windings to the assumed stack length of 108 mm, the total stack length of machine A turned out to be 146 mm and machine B turned out to be 132 mm. These numbers indicate that machine A has been made 6 mm too long and that it is possible to extend machine B by 8 mm additional. Because of time constraints and the uncertainties involved in the end-winding estimation, it was decided to keep the stator stack length according to the initial assumption of 30% extension of the 2004 Prius stator stack length.

Table 4.12: End-winding estimation using a minimum bend radius, r_{cu} , of 3 mm.

	Machine A	Machine B
W_{cu} [mm]	15.5	8.5
$2(W_{cu} + r_{cu})$ [mm]	37.0	23.00

4.2.2 Turn selection

The intention was to select the number of turns as high as possible to maximize the low speed torque without reducing the output power by voltage limitation at higher speeds. The same voltage ($225 V_{RMS}$) and current ($250 A_{RMS}$), as presented for the Prius 2004 machine in Section 3.1.1 are used as limits. Figure 4.6 and 4.7 shows possible torque speed characteristics for the two machines when varying the number of turns in five steps. 13 turns was regarded as a suitable choice for machine A and 8 turns for machine B.

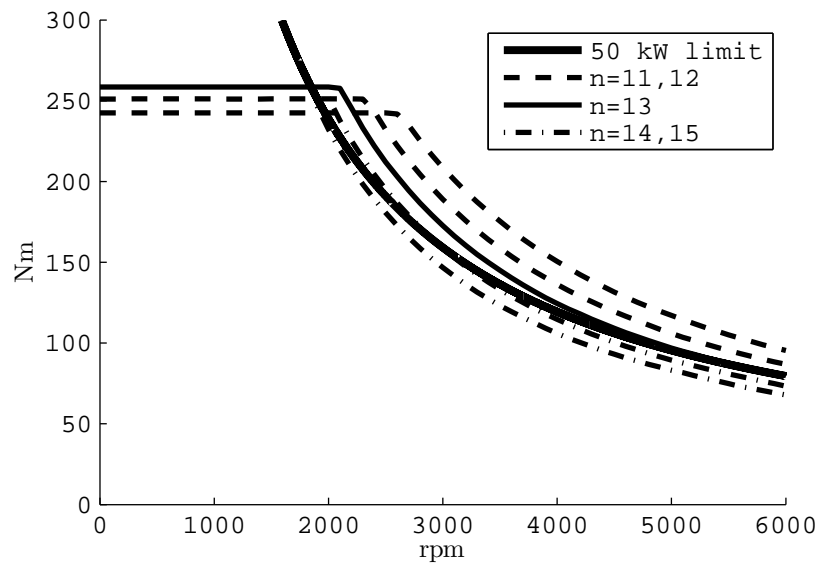


Figure 4.6: Torque speed characteristics for five different turn selections of machine A.

When taking a closer look at Figure 4.7, one can see that the output power actually is slightly limited by the voltage using the turn selection, $n=8$. The reason is that a linear model was used, in an earlier stage. When determining the number of turns and using the linear model, the voltage limit was not affecting the output torque at higher speeds. Both Figure 4.6 and 4.7 have been reproduced using dense data that was obtained in connection to the calculation of the efficiency maps shown in Section 4.3. This is also the reason why the current limited torque at lower speeds can't be seen for the higher number of turns; such high currents were not included in the data obtained in Section 4.3.

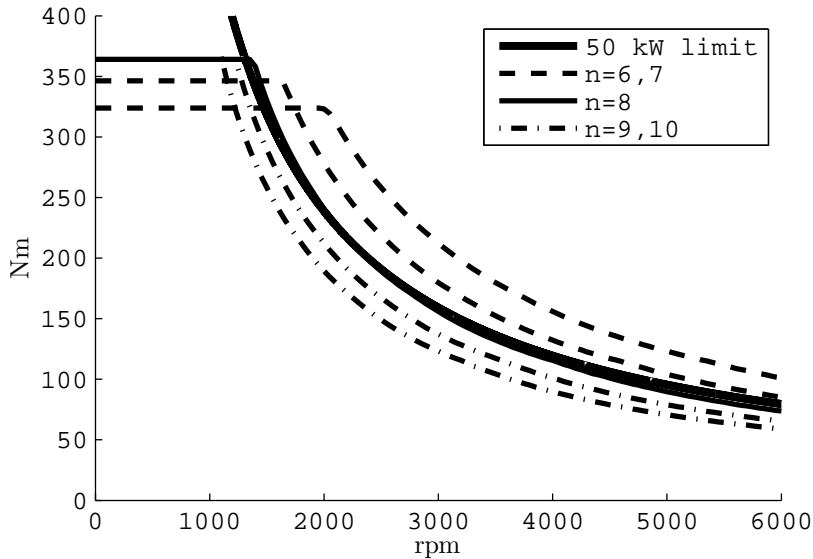


Figure 4.7: Torque speed characteristics for five different turn selections of machine B.

4.2.3 Thermal impact of the slot geometry

The thermal conductivity of the winding mix i.e. copper, insulation and impregnation is extra critical in concentrated winding fractional slot machines, as the slots are fewer and larger than in a conventional machine. Due to the larger slots and the relatively low thermal conductivity of the winding mix (compared to the stator lamination) a greater thermal gradient is expected across the winding mix inside each slot. It is necessary to achieve a high thermal conductivity of the winding mix to keep the winding temperature within adequate levels.

The thermal characteristics of two slot segments of the stator are analyzed in a somewhat simplified 2D model, one for machine A and one for the 2004 Prius slot geometry presented in [25]. The simplified geometries are shown in Figure 4.8; the air pockets in the slot openings are removed and a 0.5 mm thick and 0.2 W/(m·K) insulation film is placed between the winding mix and the stator lamination. A thermal conductivity of 28 W/(m·K) is used for the stator lamination. Insulation boundaries are used around the stator segment except for the outer boundary, representing the surface of the stator yoke, where a fixed temperature is used. The winding mix is then evenly excited by its portion of 5% copper loss in a 50 kW machine. This to show the temperature rise inside the different parts

of the stator segments relative a fixed temperature of the outer stator surface due to the copper losses.

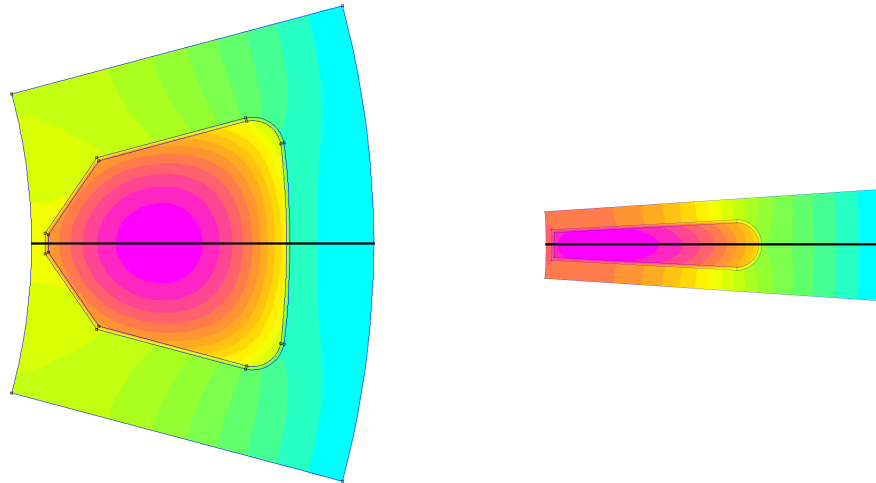


Figure 4.8: Simplified 2D geometries used to calculate relative temperature rise within a stator segment.

The distribution of the temperature rise along the black center lines in Figure 4.8 are shown in Figure 4.9. They are plotted for two different thermal conductivities of the winding mix, $0.5 \text{ W}/(\text{m}\cdot\text{K})$ and $3 \text{ W}/(\text{m}\cdot\text{K})$, for both geometries. It is clear that the thermal conductivity of the winding mix is of great importance for the maximum winding temperature of machine A; the difference is about 27°C depending on the thermal conductivity of the winding mix material. For the 2004 Prius machine, the maximum winding temperature is only affected by a few degrees.

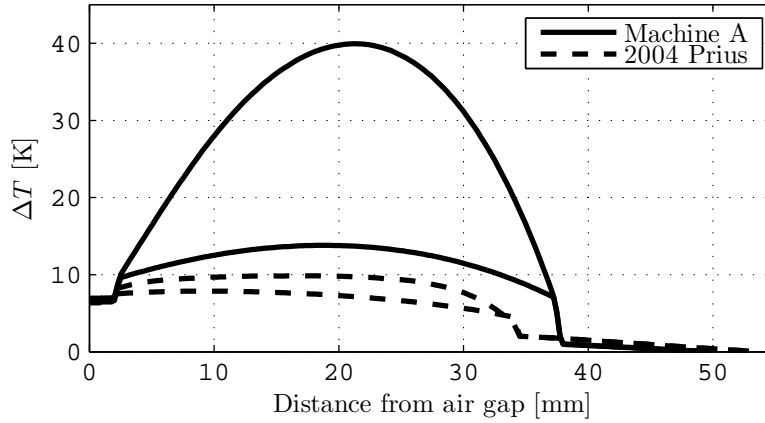


Figure 4.9: Relative temperature rise across the stator slot for two different thermal conductivities of the winding mix, 0.5 W/(m·K) and 3 W/(m·K) respectively.

4.2.4 Thermal restriction of the electric loading

The temperature distribution along a line, from the air-gap through the winding and to the outer stator yoke, was shown previously in Figure 4.9. In this section, the temperature rise at the maximum temperature along this line or the hottest spot inside a winding is calculated relative to a constant temperature at the surface of the outer stator yoke. This temperature difference is denoted ΔT_{max} and is calculated as function of the phase current for six different values of the equivalent thermal conductivity of the winding mix in the slot,

$\lambda_{w-mix}=[0.5 \ 1 \ 1.5 \ 2 \ 2.5 \ 3] \text{ W/(m}\cdot\text{K)}$. The aim is to find current density values for the two machines, A and B, and the Prius 2004 machine where the temperature rise of the windings are of the same or similar magnitude.

The relative temperature rise, ΔT_{max} , are shown for the three machines in Figure 4.10, where solid lines are used for $\lambda_{w-mix}=1.5 \text{ W/(m}\cdot\text{K)}$. One can directly conclude that machine A is the most sensitive to the thermal conductivity of the winding mix as the curves are rather spread, this is due to the relatively large slots of machine A. In the same way, the Prius 2004 machine is the least sensitive due to its relatively small slots.

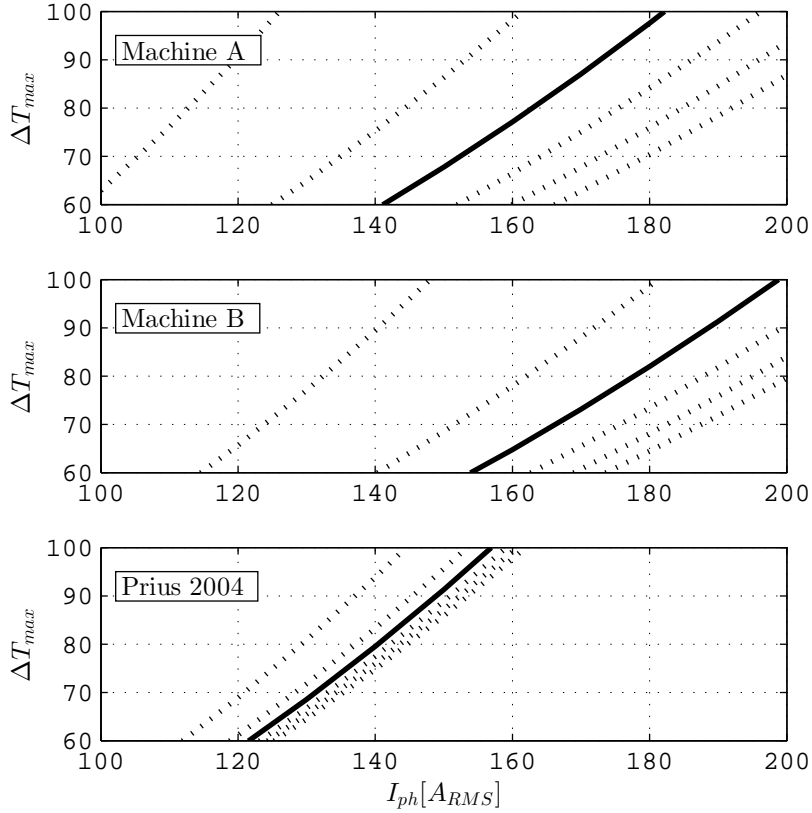


Figure 4.10: The relative temperature rise, ΔT_{max} , of the hottest spot in the winding in relation to the outer stator yoke surface as function of phase current, for different values of thermal conductivity. The solid lines correspond to an equivalent thermal conductivity of 1.5 W/(m·K) for the winding mix.

An equivalent winding mix conductivity of $\lambda_{w-mix} = 1.5$ W/(m·K) and a relative temperature rise of $\Delta T_{max} = 80^\circ\text{C}$ have been assumed as an operating point with reasonable current density levels where the three machines can be compared. The relative temperature rise of $\Delta T_{max} = 80^\circ\text{C}$ is chosen to leave some margin for additional heat flux to build up the thermal gradient further due to other loss components. This operating point should therefore not be considered as an absolute value of continuous operation.

4.3 Efficiency

Before the efficiency maps can be obtained, the operating points have to be calculated. A number of transient simulations, for different i_q and i_d combinations, were carried out for each machine. The average torque as a function of the currents, $T_{avg}(i_q, i_d)$, and the fundamental component of the stator flux as a function of the currents, $\hat{\Psi}_s^1(i_q, i_d)$, were calculated. The shortest current vector, $\min(\sqrt{i_q^2 + i_d^2})$, that fulfills the current limit, the power limit and the voltage limit is then calculated for each operating point.

The efficiency maps have been interpolated over 126 operating points made up by 9 current excitation levels and 14 speed levels, represented by the black dots in the efficiency maps. The outer black lines in the efficiency maps show the peak torque limited by current or voltage or power. The inner black lines shows the calculated torque limited by their respective $\Delta T_{max}=80^\circ\text{C}$ current, defined in the previous section.

Each operating point is simulated over two electrical periods where the losses have been calculated as an average over the last period. Core losses, P_{Fe} , of the rotors and stators are extracted directly from the FEA software together with the eddy current losses in the PMs, P_{PM} . Copper losses, P_{Cu} , are calculated in a postprocess manner using phase currents and phase resistances. The Prius 2004 phase resistance of 69 m Ω at 21 $^\circ\text{C}$ presented in [24] has been recalculated to 91.5 m Ω corresponding to the copper resistivity at 120 $^\circ\text{C}$ in Section 3.3. The phase resistances of machine A, 20.5 m Ω , and machine B, 28.1 m Ω , are calculated including the estimations of the end-windings presented in Section 4.12 and considering the copper resistivity at 120 $^\circ\text{C}$. The output power is calculated as the average torque multiplied with the mechanical speed at each operating point. The efficiency, η , in the efficiency map represents then

$$\eta = \frac{T_{avg}\Omega}{T_{avg}\Omega + P_{Fe} + P_{PM} + P_{Cu}} \quad (4.3)$$

The efficiency map of machine A can be seen in Figure 4.11, the peak torque at a phase current of $250 A_{RMS}$ is 250 Nm while the peak torque at $\Delta T_{max}=80^{\circ}C$ is 214 Nm. One can observe that the highest efficiency is obtained at relatively low torque and speed levels, as the losses are strongly dependent on both the current or flux levels and frequency.

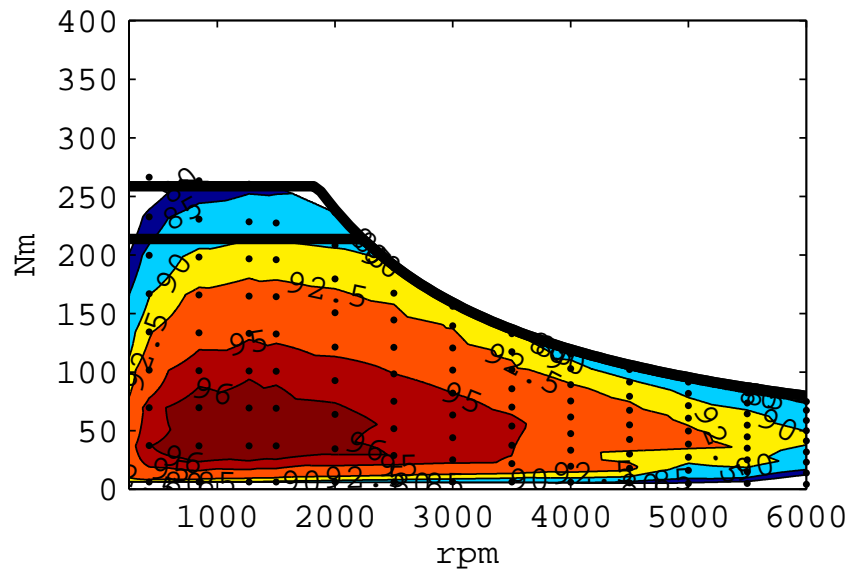


Figure 4.11: Interpolated efficiency map of machine A.

Figure 4.12 shows the efficiency map of machine B, the two black lines represents the peak torque at $250 A_{RMS}$ and at $\Delta T=80^{\circ}C$ respectively. Both the current and thermal limited torque are higher for machine B compared to machine A. Also the overall efficiency is higher, regardless of the higher pole number and the higher electric frequency.

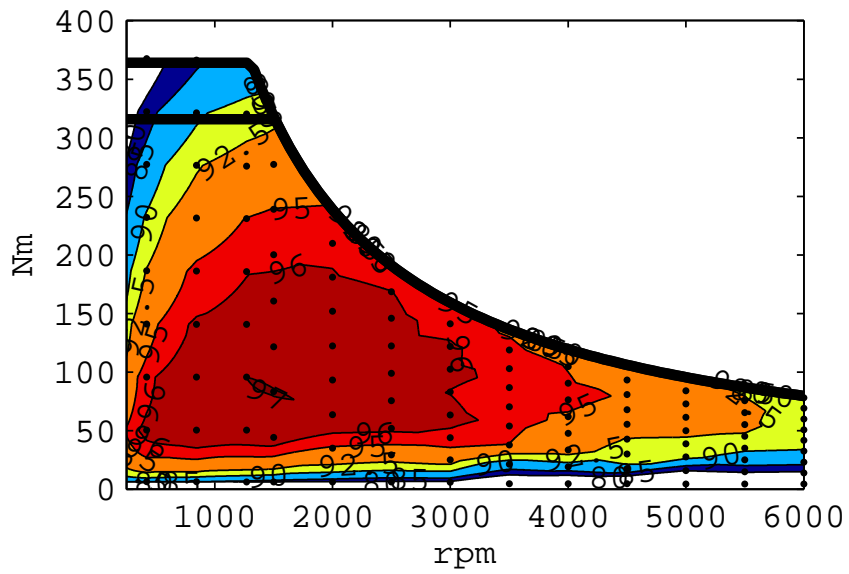


Figure 4.12: Interpolated efficiency map of machine B.

The calculated efficiency map of the 2004 Prius machine can be seen in Figure 4.13. One can notice that the efficiency is below 80% when the peak torque is delivered, the measured efficiency map in [26] shows a similar result. The overall picture when comparing the calculated and the measured efficiency maps, is that the efficiency presented in Figure 4.13 is somewhat generally higher than in [26]. The peak efficiency is also shifted from around 2250 rpm in [26] to approximately 3500 rpm in Figure 4.13. There are a number of possible sources for the discrepancy. First of all, sinusoidally shaped currents have been used when calculating the efficiency using FEA while the voltage over the measured machine has been switched. Torque measured on the machine shaft is lower than the electrodynamic torque due to mechanical losses. The exact method of how the current angle is chosen in the real system is not known, it may not be the same as the one presented in the beginning of this section. There is always an uncertainty related to the loss calculation in the simulations, especially to the core loss calculation. But there are also uncertainties involved when measuring efficiency.

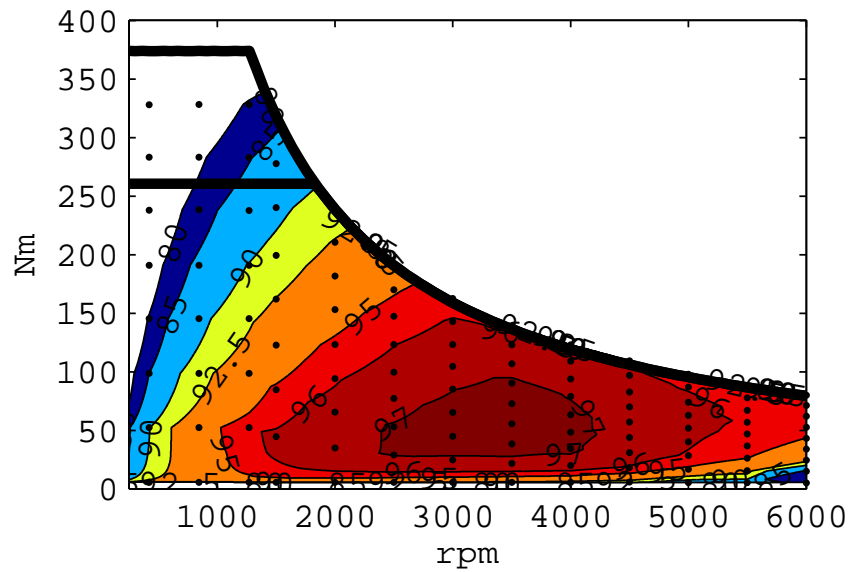


Figure 4.13: Interpolated efficiency map of the Prius 2004 machine.

4.4 Summary of comparison

Some figures from the comparison of machine A, machine B and the Prius 2004 reference machine are presented together in Table 4.13. The major difference in material consumption is that the 2004 Prius machine requires a considerable lower amount of copper and a slightly higher amount PM material. The fractional slot machine designs end up with the same material cost, which is about 8% higher than the 2004 Prius machine. Machine B and the 2004 Prius machine deliver similar torque in the current limited low speed region, while the torque production of machine A is substantially lower. The current density of the 2004 Prius is about twice the current density of machine B, which is a consequence of the relatively large end-windings and the low copper material consumption. Therefore, the torque production of machine B is considerable higher at the calculated $\Delta T_{max} = 80^\circ C$ excitation level.

Table 4.13: Some figures collected from the comparison of the three machines.

	Prius 2004	Machine A	Machine B
Outer stator diameter [mm]	269	269	269
Estimated total length [mm]	140 ¹	146 ¹	132 ¹
T_{max} [Nm]	374	258	364
$T_{\Delta T_{max} 80^\circ C}$ [Nm]	261	214	316
PM [kg]	1.232	1.050	1.178
Cu [kg]	6.8	13.739	9.776
Fe [kg]	29.25	36.51	35.79
Material cost [USD]	211	228	228
T_{max}/Cost [Nm/USD]	1.77	0.990	1.51
$T_{\Delta T_{max} 80^\circ C}/\text{Cost}$ [Nm/USD]	1.24	0.821	1.31
$J @ T_{max}$ [A_{RMS}/mm^2]	29.4	13.2	15.6
$J @ T_{\Delta T_{max} 80^\circ C}$ [A_{RMS}/mm^2]	16.5	8.6	11.1

¹See Section 4.2.1 for estimation of total lengths (stator stack + end-windings).

Chapter 5

Per phase flux machine model

This chapter presents an alternative approach to model the PMSM during unbalanced conditions. The relatively low mutual coupling between the phases are simply neglected, it is thereby made relatively easy to take the individual saturation levels of the different phases into account. The difference between the flux levels of the phases might be remarkable when one phase is operated so that its flux is enhanced while another phase is operated so that the flux is weakened. A numerical method to calculate operating points when taking the individual saturation levels, during unbalanced conditions, into account are presented in the end of the chapter.

5.1 Flux representation in a single phase

The idea of the per phase flux machine model is to utilize the fact that the fault-tolerant machine is designed to get a very low mutual coupling between the phases. If the coupling between the phases are neglected, the flux in one phase is just a function of the rotor position and the current in the phase itself. If the flux and the torque in one phase is calculated as a function of the rotor position and the current, it is possible to utilize the same 2-dimensional flux and torque maps for all the three phases by including a phase shift of the rotor position. In the stationary reference frame, the phase voltage can be expressed as

$$v_{ph} = R i_{ph} + \frac{d\psi_{ph}}{dt} \quad (5.1)$$

where the phase flux derivative can be divided into two parts, one that is related to the phase current and one that is related to the rotor position

$$\frac{d\psi_{ph}}{dt} = \frac{d\psi_i}{dt} + \frac{d\psi_\theta}{dt} \quad (5.2)$$

or linearized and expressed by quantities that are to be found in the flux map

$$\frac{d\psi_{ph}}{dt} = \frac{\Delta\psi_i}{\Delta i} \frac{di}{dt} + \frac{\Delta\psi_\theta}{\Delta\theta} \omega \quad (5.3)$$

The electrical equations, expressing the phase voltages of the three phase PMSM can be written on the same form as in (2.1), previously presented in Section 2.1. The inductance matrix has to be rewritten as

$$\mathbf{L} = \begin{bmatrix} \frac{\Delta\psi_i}{\Delta i}(i_a, \theta) & 0 & 0 \\ 0 & \frac{\Delta\psi_i}{\Delta i}(i_b, \theta - \frac{2\pi}{3}) & 0 \\ 0 & 0 & \frac{\Delta\psi_i}{\Delta i}(i_c, \theta + \frac{2\pi}{3}) \end{bmatrix} \quad (5.4)$$

where the mutual coupling between the phases are put to zero. The back EMF terms in (2.2) are reformulated as

$$\begin{bmatrix} e_a \\ e_b \\ e_c \end{bmatrix} = \begin{bmatrix} \frac{\Delta\psi_\theta}{\Delta\theta}(i_a, \theta) \\ \frac{\Delta\psi_\theta}{\Delta\theta}(i_b, \theta - \frac{2\pi}{3}) \\ \frac{\Delta\psi_\theta}{\Delta\theta}(i_c, \theta + \frac{2\pi}{3}) \end{bmatrix} \omega \quad (5.5)$$

where the individual saturation levels of the three phases during unbalanced operation will be taken into account. The instantaneous electrodynamic torque that is produced by the three phases can be calculated as

$$T_e = T(i_a, \theta) + T(i_b, \theta - \frac{2\pi}{3}) + T(i_c, \theta + \frac{2\pi}{3}) \quad (5.6)$$

where the same 2-dimensional torque map is utilized for all the three phases.

5.1.1 Per phase flux and torque maps

A great number of magnetostatic simulations were carried out, where phase A was excited in the range -360 A to +360 A while the rotor was rotated one full electrical period. In this section, the rotor angle refer to the electrical angle of phase A and zero degrees corresponds to the angle of the positive peak of the flux linkage of the PMs in phase A (positive d-axis).

The total flux-linkage, both the induced and due to the PMs, in phase A as function of rotor position and current excitation can be seen in Figure 5.1. One can observe that the current excitation is quite generous as the flux is relatively flat along the whole period of rotor positions at the highest current levels.

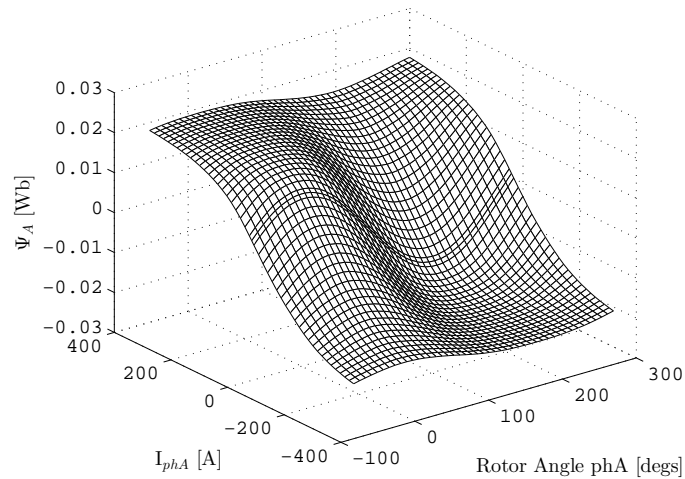


Figure 5.1: Flux-linkage in phase A as function of rotor position and phase current.

The total flux-linkage in phase C, due to the PMs and the current in phase A, is shown in the same manner in Figure 5.2. It is hard to note any difference in flux-linkage along the excitation axis, which indicates that the magnetic coupling between the phases are low.

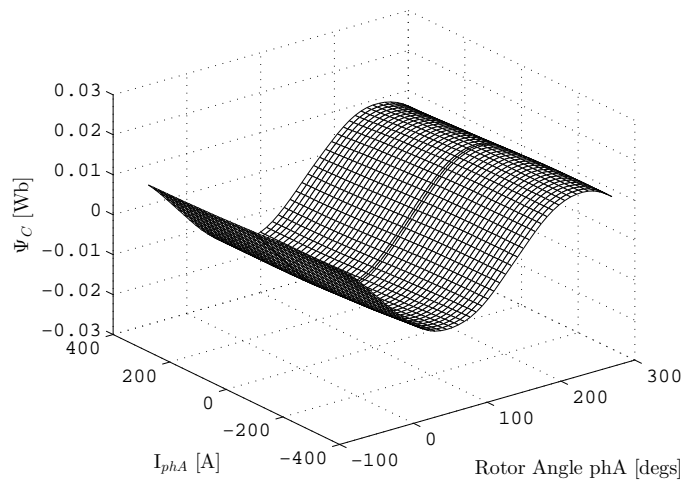


Figure 5.2: Flux-linkage in phase C as function of rotor position of phase A and current in phase A.

Figure 5.3 shows the flux-linkage in phase A when the flux-linkage at zero current is subtracted. When studying the change in flux-linkage it is clear that it is a function of rotor position and that it's not a linear function of the current. The linear region can be seen as a band that is phase shifted 180 degrees with respect to the flux-linkage of the PMs. At zero degrees, where the PM flux is at its peak, the linear band is at its minimum along the rotor angle axis.

In Figure 5.4, the flux-linkage in phase C at zero current is subtracted at each excitation level to show how much the flux-linkage in phase C is affected by the excitation of phase A. The flux-linkage is shown in the same scale as in the previous figures. When comparing Figure 5.4 and Figure 5.3, it can be observed that the change of flux linkage in the neighboring phases, B or C, due to the excitation of phase A is relatively low.

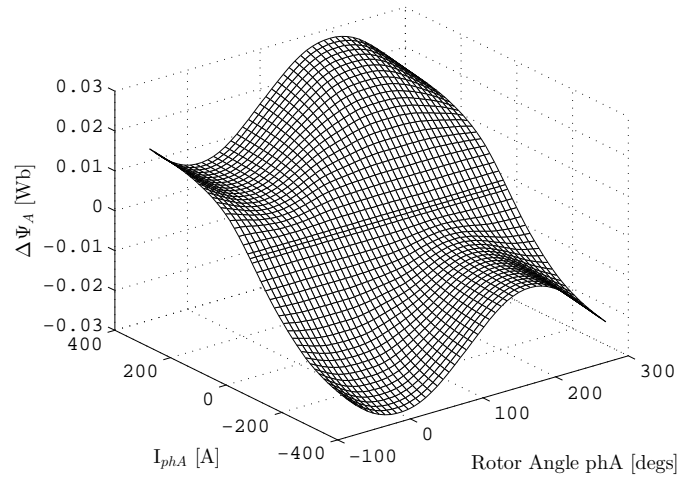


Figure 5.3: The change of flux-linkage in phase A due to the current in phase A.

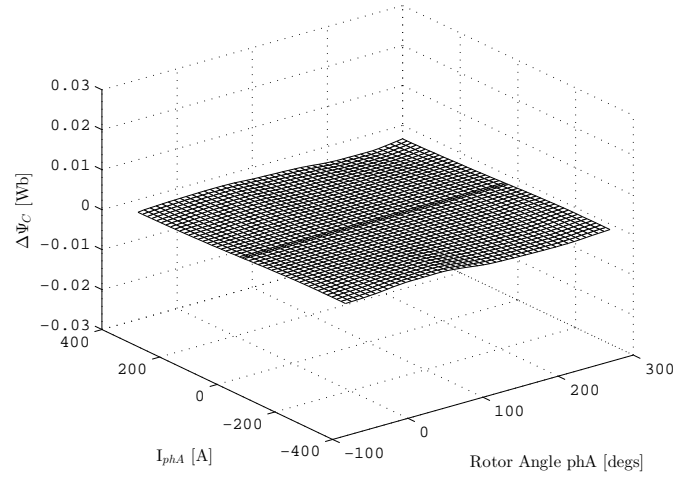


Figure 5.4: The change of flux-linkage in phase C due to the current in phase A.

Figure 5.5 shows the ratio between the change of flux-linkage in phase C and the change of flux-linkage in phase A, $|\Delta\Psi_C/\Delta\Psi_A|$ in percent, due to the current in phase A. If the the change in flux-linkage in phase A is assumed to be the total induced flux, between 2.8% and 8.6% of the total induced flux in phase A links the neighboring phases when they are unexcited. The average over the whole map, excluding the points of zero excitation, is 4.6%.

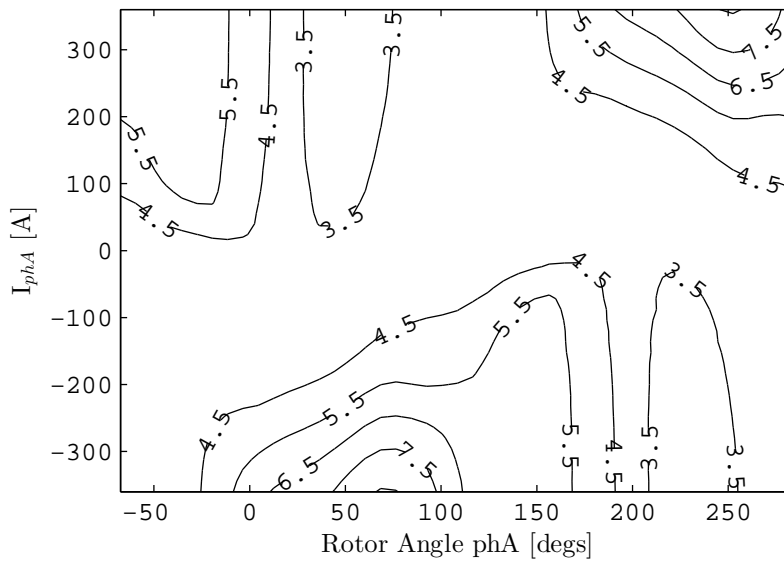


Figure 5.5: The ratio between the change in flux-linkage in phase C and the change in flux-linkage in phase A, $|\Delta\Psi_C/\Delta\Psi_A|$ in percent.

In Figure 5.6, the torque produced by a single phase as a function of its rotor position and current is shown. Excluding the highest current levels, the peak torque occur at exactly 90 electrical degrees, thus when the current is in the q-direction.

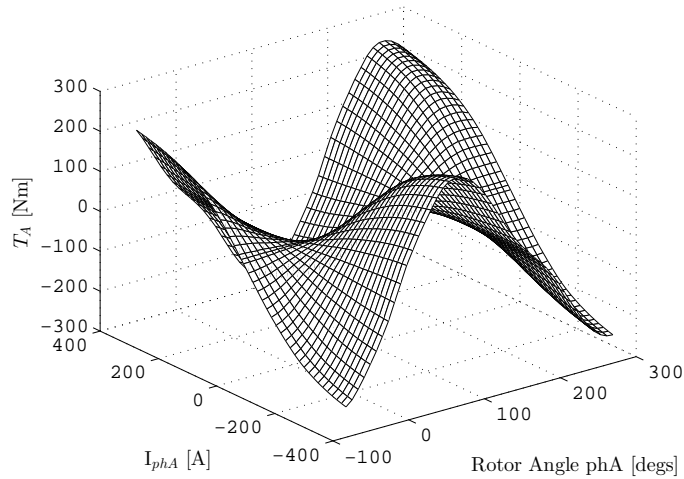


Figure 5.6: Torque production as function of rotor angle and current in phase A.

5.2 Numerical solution of 2-phase MTPA operation

A numerical method has been used to find solutions of the 2-phase MTPA operating points and it is illustrated in flow chart form in Figure 5.7. The Torque reference, T^* , is just a DC-value in case of a phase open circuit fault, as the open circuited phase doesn't produce any torque. In case of a short circuit fault, an oscillating torque reference that compensates for the torque production of the short circuited phase can be used.

The first block sorts out the combinations of phase currents, i_a and i_b , that fulfills the torque reference, $T^* \pm \Delta T^*$, according to the torque map. The combinations that minimizes $\sqrt{i_a^2 + i_b^2}$ is chosen over an electrical period. The i_a and i_b waveforms are low pass filtered using discrete Fourier transform (DFT) in order to remove unrealistically high current harmonics. The RMS values of filtered currents are calculated and compared with the maximum RMS current. If the RMS values of the calculated currents are too high, the torque reference is reduced until the current limitation criteria is fulfilled.

The phase voltages are calculated using the flux map and the currents. Another DFT is applied to the voltages to remove the higher order harmonics introduced by the discretized flux map. The peak-values of the phase voltages are compared with the maximum phase voltage. If the phase voltages are too high, the torque reference is reduced until both the current limitation criteria and the voltage

limitation criteria are fulfilled.

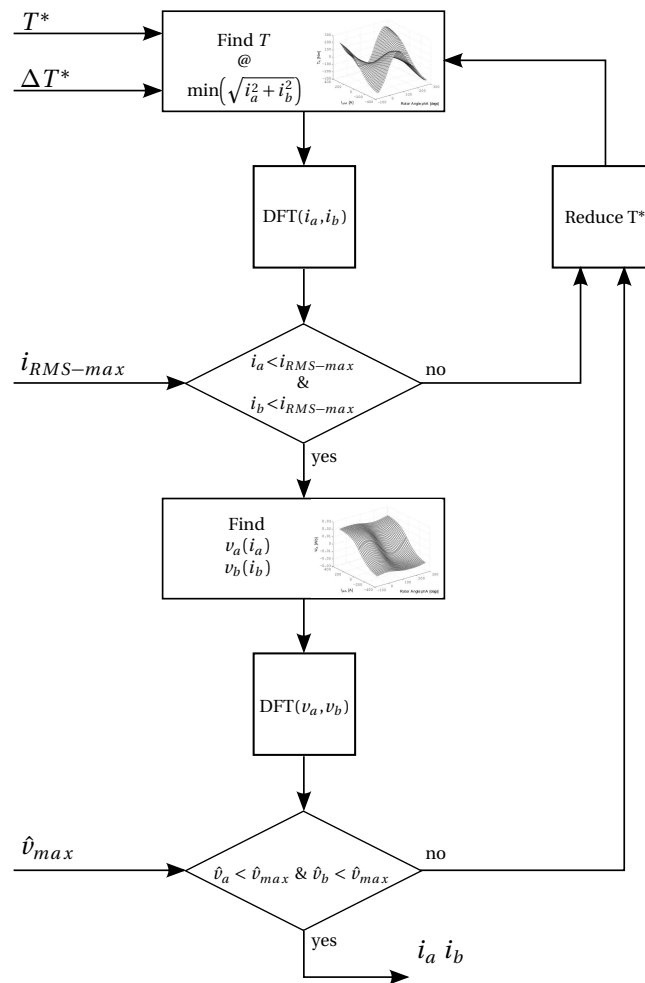


Figure 5.7: Illustration of the process that has been used find the numerical solution to the 2-phase MTPA operating point.

Chapter 6

Further analysis of one fault-tolerant fractional slot machine design

This chapter deals with the further analysis of one of the fault-tolerant PMSM machine designs that are presented earlier in this thesis. When the machine designs were evaluated in Chapter 4, machine B turned out to be a promising design and it has thus been considered in the analysis of unbalanced operation and the MMF harmonic content on the rotor side during balanced operation.

Some converter limitations related to some converter topologies were presented briefly in Section 2.5, but the constraints related to the converter topologies are not yet considered. Instead, the analysis of unbalanced operation has been made from a machine perspective, where the same phase RMS current ($250 A_{RMS}$) and the same phase peak voltage (318 V) that are available during balanced operation are just assumed to be available also during unbalanced conditions as well. The analysis has been based on two different methods; in the first method, the currents are arranged to maintain constant direct and quadrature components in the dq0 reference frame, as presented in Section 2.4.2. The first method takes only the fundamental frequency components into account and does not include the different saturation levels of the phases during unbalanced operation. Using the second method, that is based on the numerical solution of operating points presented in Section 5.2, both the difference in saturation level of the phases and several harmonic components are included.

6.1 Unbalanced operation using resonant controller

In this section, the ordinary PI controller together with the resonant controller presented in Section 2.4.2 are used to find steady-state operating points when a single phase open circuit fault or a single phase short circuit fault occurs. The operating point that was found for the single phase open circuit fault is simulated and analyzed also using transient FEA and using the per phase flux machine model described in Chapter 5.

6.1.1 Phase open circuit

The simulation that is to be analyzed is divided into three time periods, separated by the vertical dashed lines in the figures. The first part corresponds to normal operation at 1300 rpm and the current references are put to; $i_q^* = 150\sqrt{2}/3$ A and $i_d^* = 0$ A, controlled by only the PI controller. This operating point has been chosen to illustrate an example where both the phase currents and phase voltages are kept within the given boundaries. In the second part phase C is opened close to its current peak and the current is controlled down to zero as a first order system of 1 MHz bandwidth, mimicking an interruption due to a open circuit fault. During the second part, the resonant controller is still turned off and the PI controller alone, tries to reach the same current references as in the first time period. In the third and last part, the resonant controller is turned on while the current reference, i_q^* , is reduced by a factor $1/\sqrt{3}$ to end up with phase currents of the same magnitude as during the normal operation in the first time period.

As the intention is to show the three steady-states in the same figures, the controllers are tuned accordingly to achieve that. Therefore, the dynamic behavior during the two transitions between the three time periods are not representative. As an example, a_0 and a_2 of the resonant controller, see Figure 2.2, are put to zero according to [9] while a_1 is put to a value high enough to quickly remove the oscillations in i_d and i_q .

The dq0 transformation of the phase currents are shown in Figure 6.1. During normal operation, they are following their references as expected and the zero sequence component is zero as it is a balanced three phase operating point. When the fault occurs and phase C is opened, it can be seen that the PI controller alone cannot control the currents according to the references and there are oscillations in all the dq0 components. In the third time period, when the resonant controller is activated, the oscillations are removed from i_d and i_q while only i_0 is left oscillating.

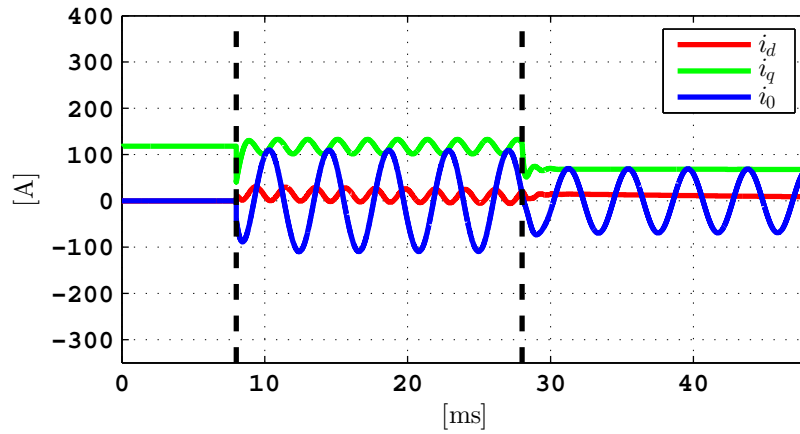


Figure 6.1: The dq0 transformation of the phase currents during normal and open circuit fault operation without and with resonant controller.

Figure 6.2 shows the phase currents during the three time periods. It can be seen that the current in phase C is interrupted when the fault occurs. In the third time period, the phase shift between phase A and B is 60 electrical degrees and both phases are shifted 30 degrees with respect to their respective phase angle during normal operation.

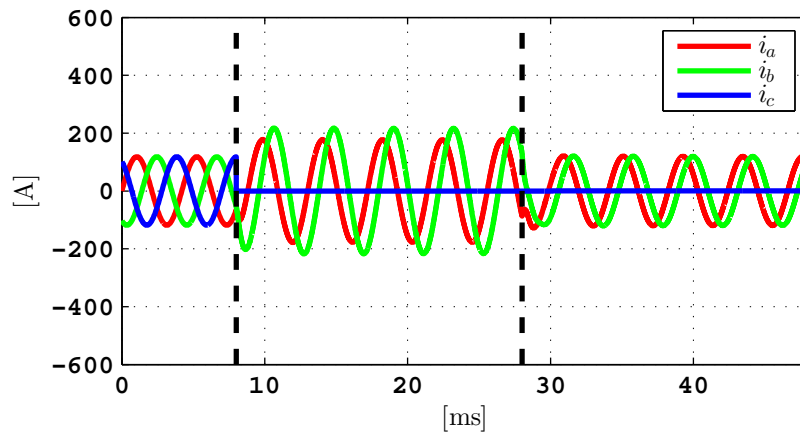


Figure 6.2: The phase currents during normal and open circuit fault operation without and with resonant controller.

The three phase voltage are presented in Figure 6.3. Considering the steady-states, it can be seen that the phase voltages are kept below $500 \cdot 2 / \pi = 318$ V at the current operating point. It can also be noted that the phase voltage of phase A is considerable higher than both phase B and C in the last time period. This is due to the fact that the current of phase A is shifted towards the PM flux vector in phase A, corresponding to a positive direct axis magnetization.

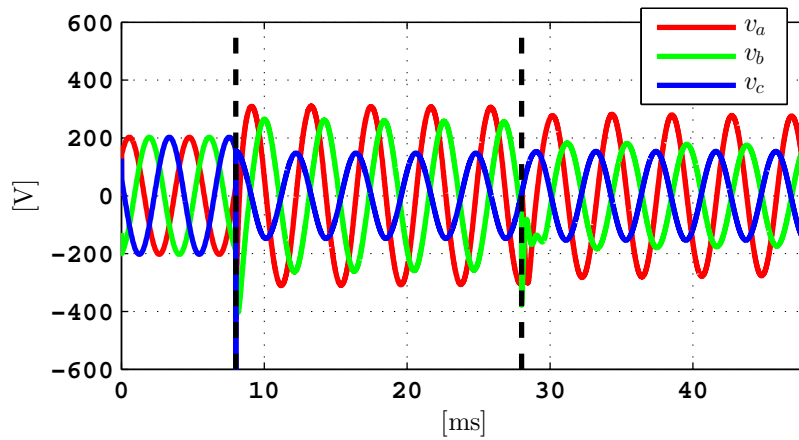


Figure 6.3: The phase voltages during normal and open circuit fault operation without and with resonant controller.

Figure 6.4 shows the torque production, the portion from each phase and the sum of the three phases. It can be seen that the oscillations in i_q and i_d give rise to oscillations also in the torque in the second time period, where the PI controller without resonant controller is used. The torque oscillations disappear when the resonant controller is activated. It can be noted that phase A and B produce sinusoidal torque components that are displaced 180 electrical degrees. This can be regarded as a fairly effective way of producing a DC torque level, because of the small amount of negative torque required.

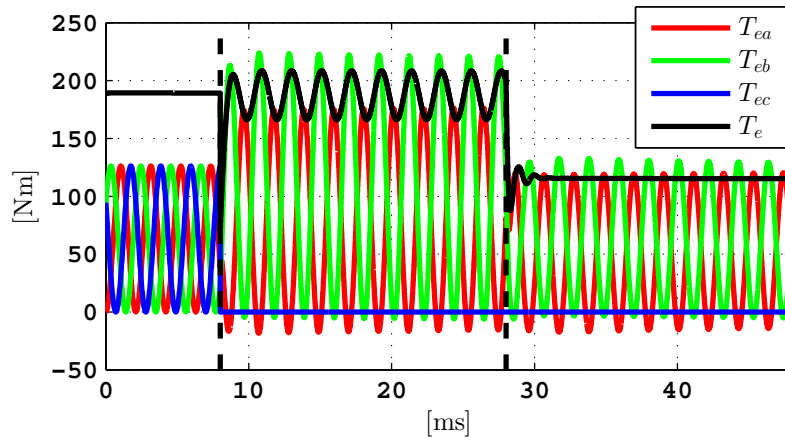


Figure 6.4: The torque production during normal and open circuit fault operation without and with resonant controller.

Comparison with FEA and the per phase flux machine model

The steady-state operating point that was found by the resonant controller previously, is simulated with the non-linear machine models; using transient FEA and using the per phase flux machine model. The phase currents for 7.5 ms of normal operation and 7.5 ms of phase open circuit operation are shown in Figure 6.5.

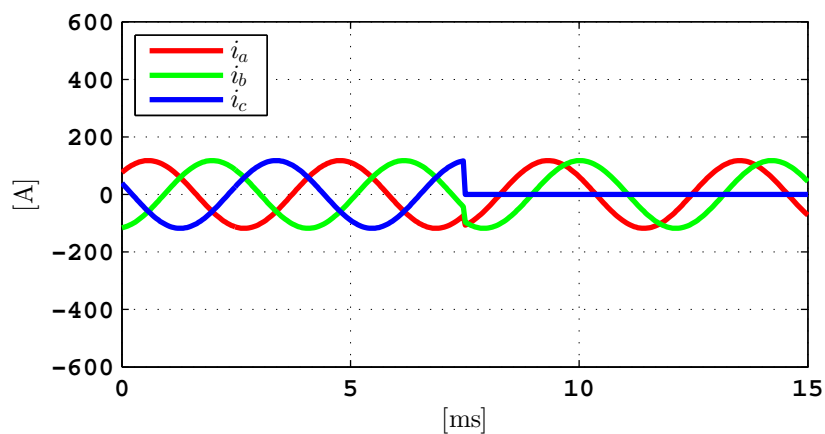


Figure 6.5: The three phase currents used as input to both the FEA and the per phase flux machine model.

The calculated torque can be seen in Figure 6.6, where the black line represents the result from the transient FEA. In this specific operating point, the ripple torque during normal operation is approximately 5% of the average torque while it is around 25% when the machine is operated during open circuit fault. The torque that has been calculated using the per phase flux machine model gives a result that is very close to the transient FEA. It can be seen that additional torque ripple is introduced when the non linear machine models are excited to keep the resulting quadrature component of the current constant.

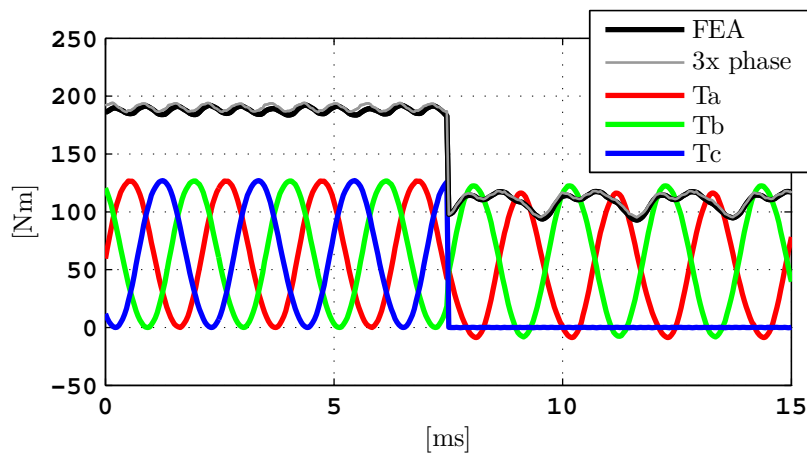


Figure 6.6: Torque production during 7.5 ms of normal operation and 7.5 ms of phase open circuit operation.

The three phase voltages obtained by the FEA and the per phase flux machine model are shown in Figure 6.7. It is hard to distinguish the results and the voltages are distorted, especially when the machine is operated during open circuit fault. The voltages during the last 7.5 ms are to be compared with the third time period in Figure 6.3. It is clear that phase A is the most distorted, as the current in phase A produces induced flux that enhances the PM flux while the current in phase B induces flux that weakens the PM flux.

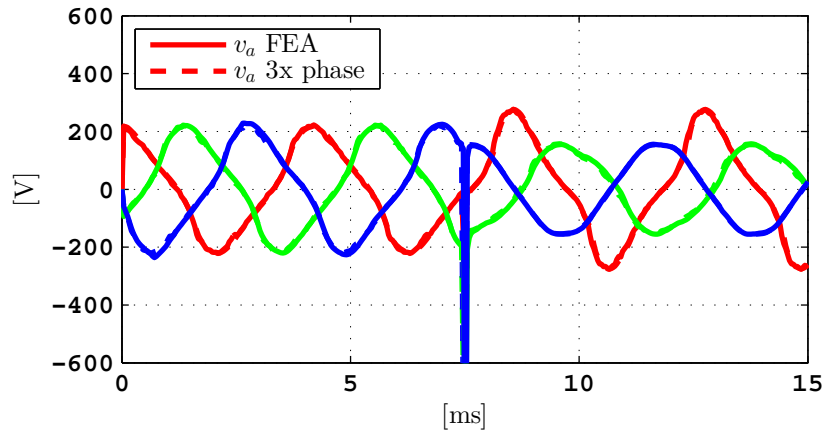


Figure 6.7: Phase voltages during 7.5 ms of normal operation and 7.5 ms of phase open circuit operation.

6.1.2 Phase short circuit

This section shows the event of a phase short circuit fault in the same manner as the open circuit fault in the previous section. Both the same operation point and the same controller reaction are considered. The only difference is that the terminal voltage of the faulty phase (C) is instantaneously put to zero, instead of controlling the phase current to zero.

The dq0 transformation of the phase currents are shown in Figure 6.8, it can be seen that oscillations are introduced in all the dq0 components when phase C is short circuited. When the resonant controller is activated, the oscillations are removed from i_d and i_q again.

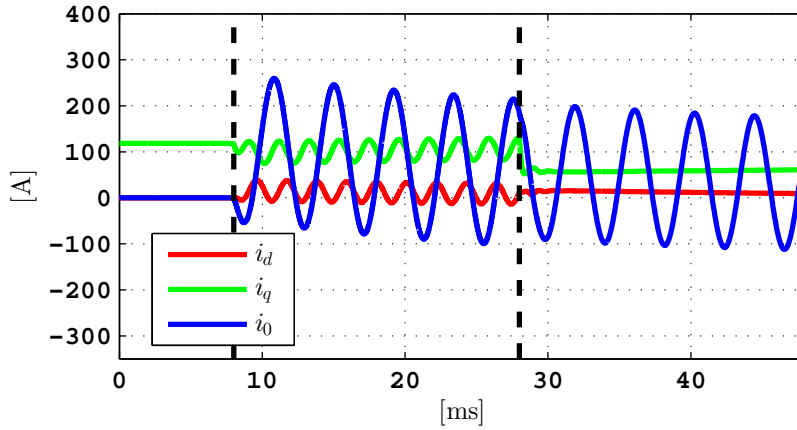


Figure 6.8: The dq0 transformation of the phase currents during normal and short circuit fault operation without and with resonant controller.

The three phase currents are presented in Figure 6.9 and some critical changes can be observed. First of all, there is current in phase C as it is short circuited. The short circuit current is limited to about $84 A_{RMS}$ by the impedance of the phase, mainly the inductance. The current in the faulty phase will introduce an additional torque component compared with the case of an open circuit fault. The final steady-state cannot be seen in Figure 6.9 but the phase shift between phase A and B will end up to around 35 electrical degrees for this particular operating point. As a consequence, this operating point is even further away from the balanced case, compared with the open circuit fault. The phase current of both phase A and C end up with approximately the same amplitudes as during normal operation, while the amplitude of phase B is increased by 76% to maintain the current reference, i_q^* , that is still reduced by a factor $1/\sqrt{3}$.

The torque production of the three phases during normal and short circuit operation are shown in Figure 6.10. It can be observed that there are a lot of oscillations in the torque and that there are a considerable amount of negative torque that is produced. One can conclude that the control strategy, using the PI and the resonant controller and only utilizing the fundamental frequency, to maintain a DC torque level is not that strategic; a great portion of the torque produced by phase A and B cancel out each other.

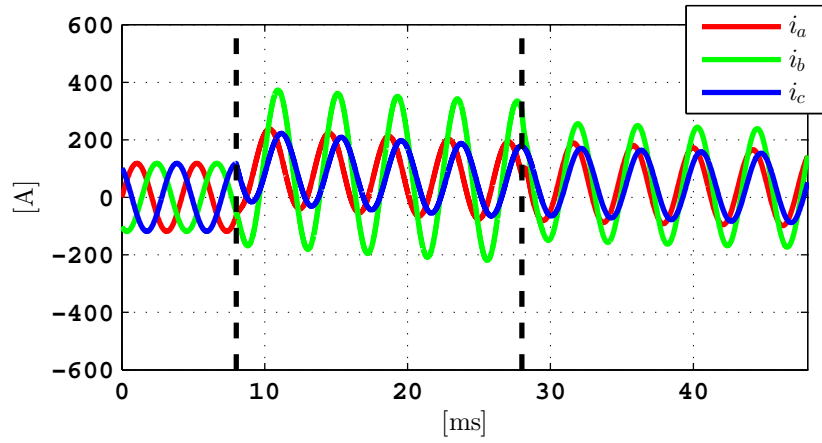


Figure 6.9: The phase currents during normal and short circuit fault operation without and with resonant controller.

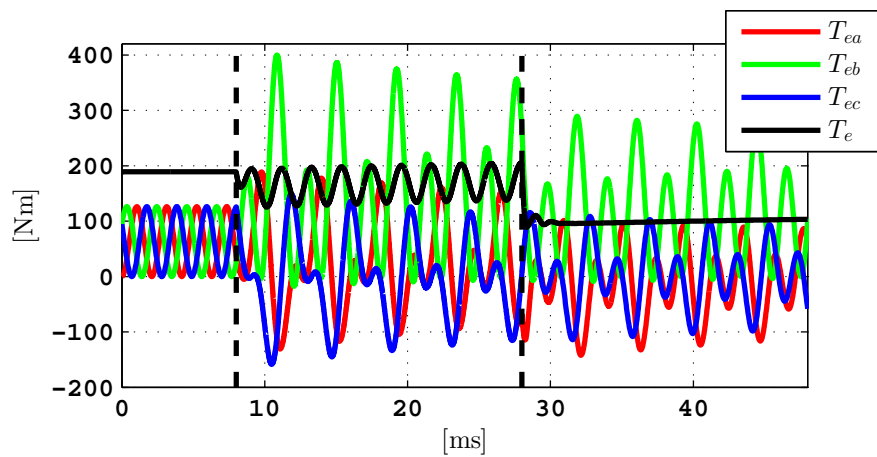


Figure 6.10: The torque production during normal and short circuit fault operation without and with resonant controller.

6.2 Numerically calculated unbalanced operating points

This section is based on the per phase flux machine model that was introduced in Chapter 5. The impact of harmonic content in the currents are analyzed and torque speed characteristics during a phase open circuit fault and a phase short circuit fault are evaluated.

6.2.1 Filtering of numerically calculated currents

In the flowchart, presented in Figure 5.7, it was shown that the shortest current vector, $\min(\sqrt{i_a^2 + i_b^2})$, for a given Torque reference, T^* , is calculated based on a torque map. The calculated current waveforms are then low pass filtered using a discrete Fourier transform (DFT) in order to remove unrealistically high harmonics. It is therefore of interest to analyze the magnitude of the torque ripple that is introduced as a consequence of the filtering. The peak to peak torque ripple expressed relative to the average torque in percent is presented in Figure 6.11 for different number of harmonics.

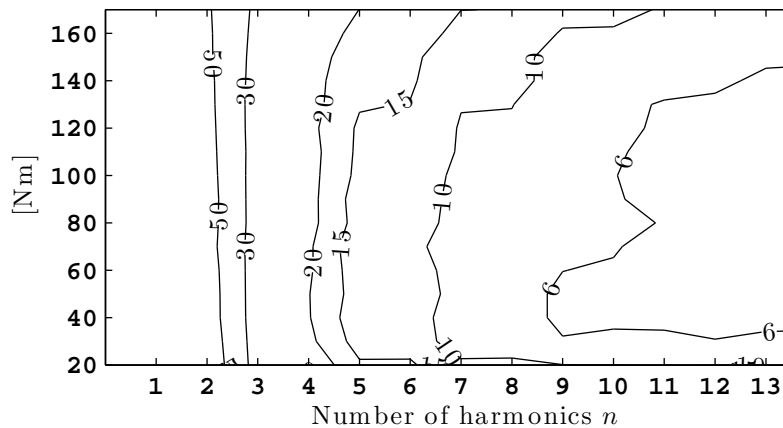


Figure 6.11: Peak to peak torque ripple expressed relative to the average torque in percent for different number of harmonics.

A choice of how many harmonics to include in the currents is a trade-off between torque quality and other constraints. The torque ripple is of course reduced with an increased harmonic content as seen in Figure 6.11, but higher harmonic content will likely increase the losses. Higher voltage may be required when the harmonic content of the current is increased, thereby is it possible that the speed will be further limited for a certain DC-link voltage. The controller bandwidth is another aspect to consider with a higher harmonic content.

A torque ripple of 10-15% in the interval 20-170 Nm is assumed to be reasonable, why a harmonic content of $n=7$ has been chosen.

6.2.2 Torque speed characteristics

The torque speed characteristics of machine B, when using two different numbers of harmonic content, during phase open circuit fault is presented in Figure 6.12. The current limited low speed torque is 175 Nm, which is about 17% lower than the theoretical limitation presented in Section 2.5 ($364/\sqrt{3}=210$ Nm). The torque reductions start at 400 rpm and 600 rpm respectively. At 2000 rpm, the torque production has dropped to 53 Nm and 62 Nm respectively and it decreases fast until it becomes zero at about 2600 rpm.

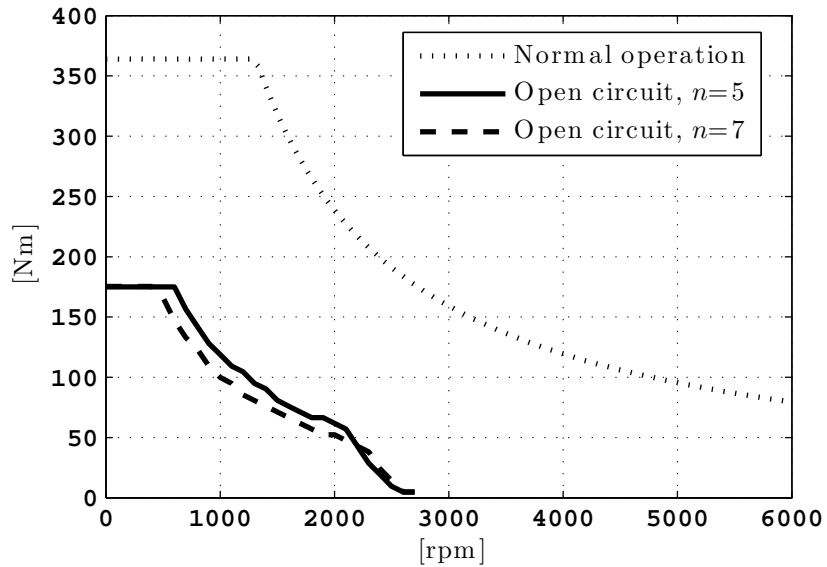


Figure 6.12: Torque speed characteristics of machine B during open circuit fault.

In Figure 6.13, the torque speed characteristics of machine B during phase short circuit operation is shown. The torque production is calculated for two different numbers of harmonic content, a local minimum at around 40 rpm can be seen in both cases. The local minimum coincide with the maximum of the braking torque produced by the short circuited phase C, see $|T_{c-avg}|$ in Figure 6.13. The speed levels, where the torque must be reduced are actually slightly higher than in the case of the open circuit fault, 600 rpm and 700 rpm respectively. After that, the torque is reduced faster compared with the open circuit fault. The

remaining phases must not only produce the DC torque level, they must also compensate for the oscillating torque produced in the short circuited phase.

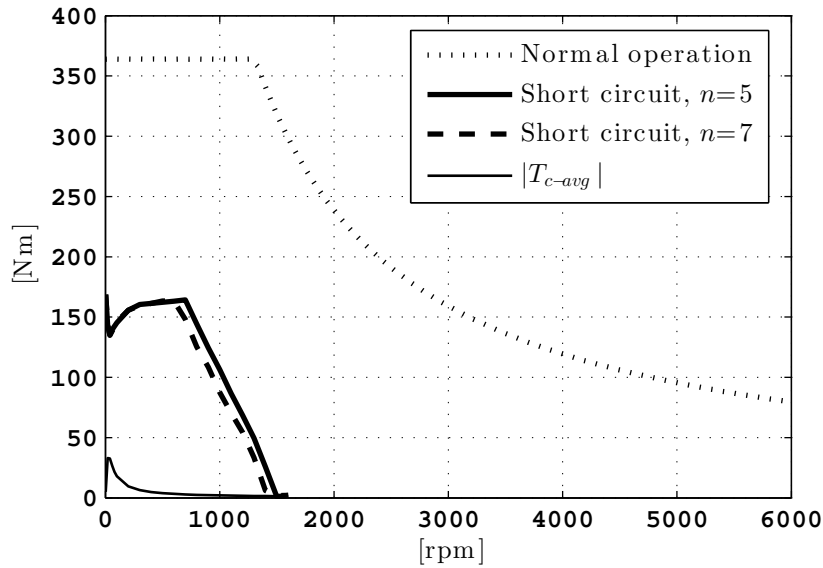


Figure 6.13: Torque speed characteristics of machine B during short circuit fault.

At a speed around 600-700 rpm, the braking torque, $|T_{c-avg}|$, is relatively low, the torque produced by the short circuited phase is just oscillating around zero. As a higher speed is reached before the torque must be reduced compared with the open circuit fault, it can be concluded that oscillating torque helps the remaining phases to maintain the DC torque level. For the strategy used, with the filtering of the ideal MTPA operating points, it is beneficial to utilize the positive part and to cancel the negative part of the oscillating torque compared to producing the whole DC torque level as in case of an open circuit fault. At least, if considering only the torque level at this particular speed.

6.2.3 Efficiency

The calculated efficiency map for machine B, interpolated over 81 operating points, when operated during phase open circuit fault can be seen in Figure 6.14. The operating points are calculated according to the numerical method presented in Section 5.2 (the per phase flux machine model), where harmonics up to $n=7$ are included in the phase currents. Each operating point (of input currents at a given speed) is simulated using transient FEA and the losses and torque at a given speed are calculated in the same way as presented in Section 4.3. Thus, the outer black line in the efficiency map shows the peak torque limited by current or voltage when $n=7$, calculated with the per phase flux machine model, and the efficiency map and the black points are results from the transient FEA. The efficiency during open circuit fault is lower compared with the normal operation, previously presented in Figure 4.12 in Section 4.3. This is expected since one third of the machine is somehow deactivated, while the remaining two thirds are pushed harder and harmonics are introduced to reduce the torque ripple.

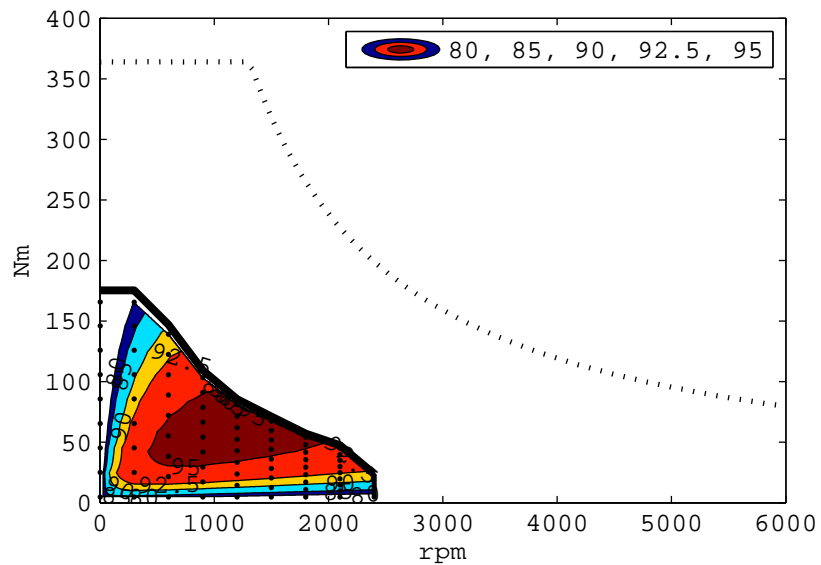


Figure 6.14: Efficiency map of machine B during open circuit operation.

The calculated efficiency map of machine B, when operated during short circuit fault, is presented in Figure 6.15. It is interpolated over 90 operating points and harmonics up to $n=7$ are included in the phase currents, which are sim-

ulated using transient FEA. The efficiency when operating during short circuit fault is even lower than in the case of an open circuit fault, which is expected since there are additional losses in the short circuited phase and the remaining phases are pushed even harder. One can also observe a discrepancy of about 6 % in the maximum torque between the per phase flux machine model and the transient FEA. The discrepancy could be caused by both the fact that the phases are not completely decoupled and the discretization of the per phase flux machine model.

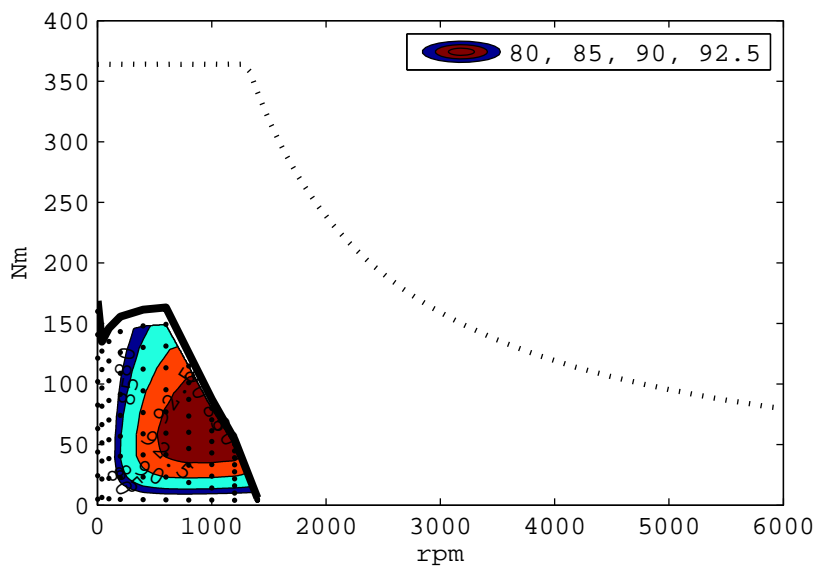


Figure 6.15: Efficiency map of machine B during short circuit operation.

6.3 2D modeling of MMF harmonic content and losses on the rotor side

In Figure 6.16, the harmonic content in magnetic field over the air-gap, the flux and current on the rotor side are shown. The amplitudes are calculated in two different ways and are normalized around their respective $f_{rn}/f = 2^2/11$ component. The MMF harmonic content is calculated analytically in the same way as when Figure 3.3 and Figure 3.4 were obtained. The radial component of the flux density, B_r , and the axial component of the current density, J_z , are calculated using FEA. B_r is extracted in a point close to the rotor surface and J_z is extracted 2 electrical degrees from a PM edge. It is clear that the analytically predicted harmonic content is seen also in the FEA. The individual amplitudes of the flux densities are not exactly the same as in the MMF wave, which is an expected result as the reluctance seen by different wave-lengths are not the same. In the same manner, the current path for different wave-lengths is not the same. From the result presented in Figure 6.16, it is not possible to directly determine which harmonics that create the highest losses, as they are only evaluated in single points. To divide the losses produced by different harmonics, each frequency component must be calculated and integrated separately over the whole surface of the 2D object of interest.

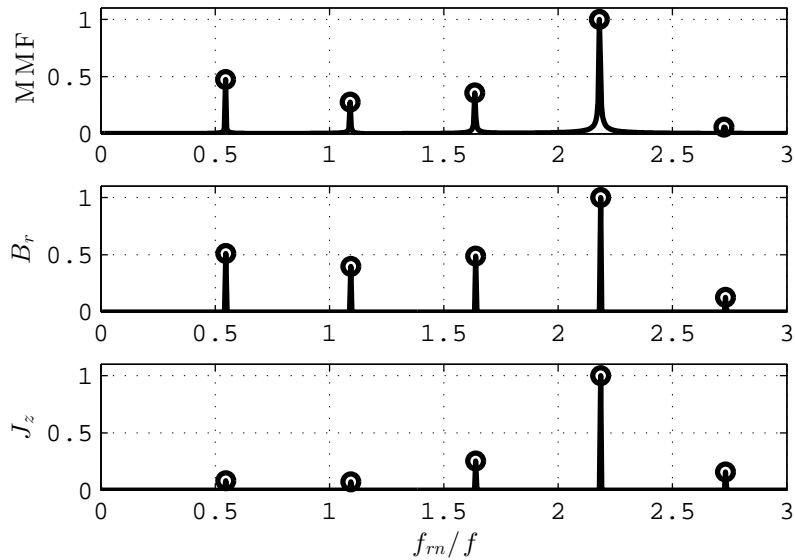


Figure 6.16: Harmonic content on the rotor side of machine B.

It should be mentioned that the induced eddy currents in the PMs flow in three dimensional current paths and that 3D modeling is required for correct eddy current loss calculations. However, the computational time needed to solve the 3D problems with a reasonable mesh resolution within the PMs was not possible to fit into the limited time frame of this licentiate work. The eddy current losses and segmentation of the PM have, so far, been studied in 2D only. In the FEA, the PMs are treated as solid objects with a certain bulk conductivity. Current can flow freely in the axial direction of a PM but the sum of the current in the axial direction of a single PM must be zero. Since it is defined as a 2D problem, it is not possible to segment the PMs in the axial direction. The PMs are therefore segmented in the circumferential direction only.

The total PM loss was calculated at the maximum torque at 14 different speeds, shown in Figure 6.17. It is clear that the PM losses are increased with both frequency and current, as the losses are lowered when the current is reduced due to the power limit at 1270 rpm. It can be seen that the very high total losses are reduced drastically when each PM is segmented into two parts. Even when going from two parts to three, the losses are reduced almost 50% while the difference in the last step is about 30 %.

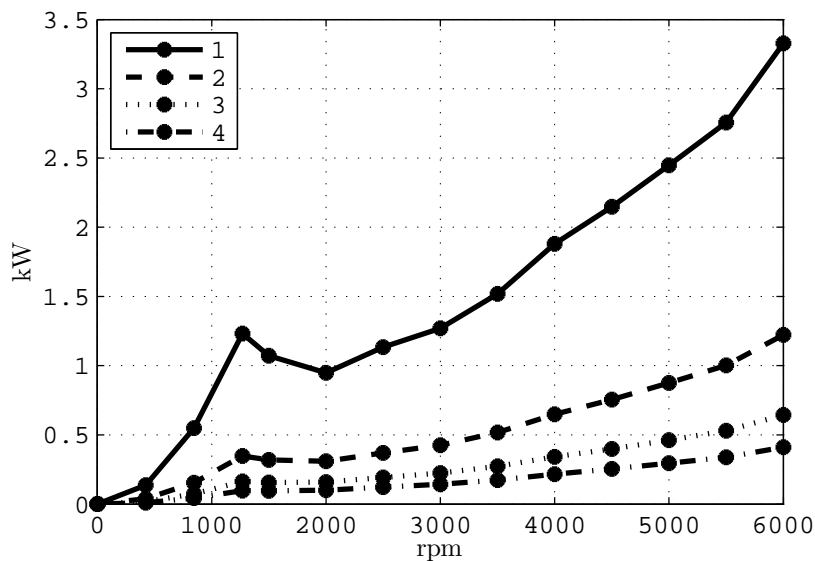


Figure 6.17: Total PM loss in machine B, when each PM consists of 1-4 equally sized pieces.

From Figure 6.17, it is obvious that the losses that are calculated in the solid PM using 2D FEA is unrealistically high in a practical sense. The efficiency map that is presented in Figure 4.12 in Section 4.3 using solid PMs, were therefore reproduced using segmented PMs. The efficiency map over machine B, when the PMs are divided into four equally sized pieces is shown in Figure 6.18. The maximum efficiency is achieved at a higher frequency compared with the previous case with solid PMs. It can also be noticed that the peak torque is reduced slightly due to the segmentation. The area corresponding to an efficiency above 97% is even larger than calculated for the 2004 Prius machine, presented in Figure 4.13.

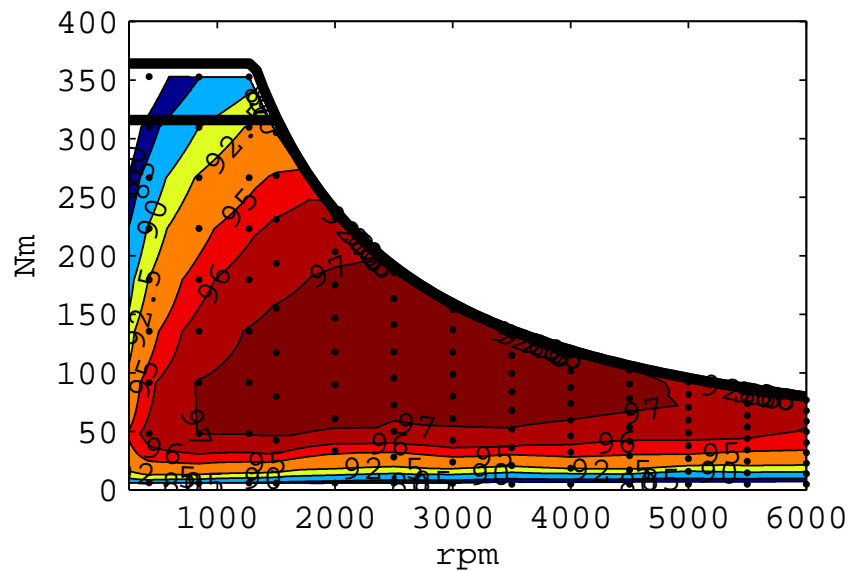


Figure 6.18: Interpolated efficiency map of machine B, when the PMs are divided into four equally sized pieces.

Chapter 7

Conclusions and future work

7.1 Conclusions

In this thesis, a fault-tolerant fractional slot machine with a similar size and performance as the Toyota Prius 2004 reference machine is designed. The faults investigated are phase open circuit and phase short circuit, and it is shown that the thesis machine design can be operated during both circumstances. The electromagnetic design of the machines have been compared with the use of 2D finite element analysis; the calculated overall efficiency of the final thesis design turned out to be slightly higher than that of the 2004 Prius design, in case of segmented permanent magnets. The estimated material cost to produce a machine is included already in the design process, where four design variables are varied. In that way, the most promising designs considering both performance and cost were sorted out. The estimated material cost of the finally selected machine design is about 8% higher and the peak torque slightly lower (364 Nm) than the 2004 Prius design (374 Nm).

It has been shown that the torque ripple of a PMSM may increase when operated under unbalanced conditions and the phase currents are controlled in the classical vector control manner to maintain a constant torque producing quadrature axis current in the dq0 reference frame. A semi-analytical machine modeling approach is used to model the individual saturation levels of the phases successfully. Harmonics can be included in the phase currents to increase the torque quality but the area of possible operating points is reduced substantially. The maximum torque is reduced by approximately 50% and can be maintained up to about 600 rpm in case of an open circuit fault, compared to about 1300 rpm at normal operation. In case of a short circuit fault, the maximum torque varies within the whole speed operating range, due to the braking torque produced by the short circuited phase. The starting torque, when the short circuit torque is

negligible, is of course reduced to approximately 50% also in case of a short circuit fault. Without a constant speed load profile, it is not possible to determine the reduction of the maximum vehicle speed; but in rough numbers about 1/3 or slightly below 1/4 of the maximum speed of 6000 rpm during normal operation, in case of an open circuit fault or a short circuit fault respectively, is what is achievable.

7.2 Future Work

Here follow some suggestions for future work, either parts that were consciously not included in this work or as reflection over the thesis and its results.

- When the cost efficiency of the electric machine designs were evaluated, only the torque production at low speed was included. It is possible to improve the process by adding more properties in order to sort out the most promising candidates in a more effective manner. For example, the field weakening characteristics and the thermal restrictions of electric loading could be evaluated at the same time. It is also possible to reformulate the constraint instead of using a single break point of above 95% of the maximum torque output per cost.
- Investigate the effect of the DC-link current ripple in relation to both performance and comfort when operating during fault.
- Model the eddy current loss in the permanent magnets and evaluate segmentation using 3D finite element analysis, both during normal operation and operation during a fault.
- Further thermal analysis, using less simplified models.
- Complete electric drive system modeling including both machine and converter models but also the control and fault detection.
- There are commercial fractional slot concentrated winding PMSM available on the market, some of them are potentially of suitable pole/slot configurations for unbalanced operation during fault. That would be interesting to investigate and test in the lab.
- Compare the results with other fault-tolerant solutions; it could be multi-phase systems with a separate converter and machine or modular systems where the winding terminals are attached directly to the power electronics.
- Combine an electric drive system model with a vehicle model in order to evaluate fault-tolerant vehicle performance more precisely.
- Analyze how the machine performance during fault is affected in case of a PMSM with interior-mounted permanent magnets instead of surface-mounted permanent magnets.

Bibliography

- [1] D. Diallo, M. Benbouzid, and A. Makouf, "A fault-tolerant control architecture for induction motor drives in automotive applications," *Vehicular Technology, IEEE Transactions on*, vol. 53, no. 6, pp. 1847–1855, Nov 2004.
- [2] A. Jack, B. Mecrow, and J. Haylock, "A comparative study of permanent magnet and switched reluctance motors for high-performance fault-tolerant applications," *Industry Applications, IEEE Transactions on*, vol. 32, no. 4, pp. 889–895, Jul 1996.
- [3] N. Bianchi and S. Bolognani, "Fault -tolerant pm motors in automotive applications," in *Vehicle Power and Propulsion, 2005 IEEE Conference*, Sept 2005, pp. 747–755.
- [4] M. Abolhassani and H. Toliyat, "Fault tolerant permanent magnet motor drives for electric vehicles," in *Electric Machines and Drives Conference, 2009. IEMDC '09. IEEE International*, May 2009, pp. 1146–1152.
- [5] A. EL-Refaie, "Fractional-slot concentrated-windings synchronous permanent magnet machines: Opportunities and challenges," *Industrial Electronics, IEEE Transactions on*, vol. 57, no. 1, pp. 107–121, Jan 2010.
- [6] E. Fornasiero, *Advanced Design of Direct Drive PM Machines*. Ph.D. thesis, Department of Electrical Engineering, University of Padova, Padova, Italy, 2010.
- [7] G. Dajaku and D. Gerling, "Low costs and high-efficiency electric machines," in *Electric Drives Production Conference (EDPC), 2012 2nd International*, Oct 2012, pp. 1–7.
- [8] M. Barcaro, N. Bianchi, E. Fornasiero, and F. Magnussen, "Experimental comparison between two fault-tolerant fractional-slot multiphase pm motor drives," in *Industrial Electronics (ISIE), 2010 IEEE International Symposium on*, July 2010, pp. 2160–2165.

- [9] Y. Crevits, X. Kestelyn, and E. Semail, "Investigation on vector control of three-phase synchronous machines under supply fault condition," in *Power Electronics, Electrical Drives, Automation and Motion, 2006. SPEEDAM 2006. International Symposium on*, May 2006, pp. 439–444.
- [10] C. Gajanayake, B. Bhangu, S. Nadarajan, and G. Jayasinghe, "Fault tolerant control method to improve the torque and speed response in pmsm drive with winding faults," in *Power Electronics and Drive Systems (PEDS), 2011 IEEE Ninth International Conference on*, Dec 2011, pp. 956–961.
- [11] N. Bianchi, S. Bolognani, M. Zigliotto, and M. Zordan, "Innovative remedial strategies for inverter faults in ipm synchronous motor drives," *Energy Conversion, IEEE Transactions on*, vol. 18, no. 2, pp. 306–314, June 2003.
- [12] N. Bianchi, S. Bolognani, and M. Zigliotto, "Analysis of pm synchronous motor drive failures during flux weakening operation," in *Power Electronics Specialists Conference, 1996. PESC '96 Record., 27th Annual IEEE*, vol. 2, Jun 1996, pp. 1542–1548 vol.2.
- [13] A. Krings and J. Soulard, "Overview and comparison of iron loss models for electrical machines," *Journal of Electrical Engineering*, vol. 10, no. 3, pp. 162–169, 2010, updated and revised version of conference paper from the 5th International Conference and Exhibition on Ecological Vehicles and Renewable Energies (EVER 10), Monte-Carlo, MONACO, MAR 25-28, 2010QC 20120120.
- [14] L. Svensson, M. Andersson, A. Reinap, and M. Alaküla, "Thermal properties on high fill factor electrical windings: Infiltrated vs non infiltrated," *International Conference on Electrical Machines (ICEM14), Berlin, Germany*, Sep 2014.
- [15] A. Jack, B. Mecrow, P. Dickinson, D. Stephenson, J. Burdess, J. N. Fawcett, and T. Evans, "Permanent magnet machines with powdered iron cores and pre-pressed windings," in *Industry Applications Conference, 1999. Thirty-Fourth IAS Annual Meeting. Conference Record of the 1999 IEEE*, vol. 1, 1999, pp. 97–103 vol.1.
- [16] R. Wrobel, P. Mellor, and D. Holliday, "Thermal modeling of a segmented stator winding design," *Industry Applications, IEEE Transactions on*, vol. 47, no. 5, pp. 2023–2030, Sept 2011.
- [17] H. J.R. and M. T.J.E, *Design Of Brushless Permanent-Magnet Machines*. Motor Design Books LLC, Florida, 2010.
- [18] J. Gieras, M. Kamper, and R.-J. Wang, *Axial Flux Permanent Magnet Brushless Machines 2nd Edition*. Springer Science & Business Media B.V., 2008.

- [19] C. Liwschitz-Garik, M. assisted by Clyde and E. Whipple, *Electric Machinery, Volume 2 A-C Machines*. Van Nordstrand, New York, 1946.
- [20] G. Dajaku, D. Gerling, and W. Xie, "Reduction of low space harmonics for the fractional slot concentrated windings using a novel stator design," *Magnetics, IEEE Transactions on*, vol. PP, no. 99, pp. 1–1, 2013.
- [21] T. D. Strous, H. Polinder, and J. Ferreira, "Inductance calculations for pm machines with concentrated windings," in *Electric Machines Drives Conference (IEMDC), 2011 IEEE International*, May 2011, pp. 447–452.
- [22] R. Krishnan, *Permanent Magnet Synchronous and Brushless DC Motor Drives*. Hoboken: CRC Press, 2009. [Online]. Available: www.summon.com
- [23] L. Chong, R. Dutta, N. Dai, M. Rahman, and H. Lovatt, "Comparison of concentrated and distributed windings in an ipm machine for field weakening applications," in *Universities Power Engineering Conference (AUPEC), 2010 20th Australasian*, Dec 2010, pp. 1–5.
- [24] T. A. O. Burress, S. L. O. Campbell, C. O. Coomer, C. W. O. Ayers, A. A. O. Wereszczak, J. P. O. Cunningham, L. D. O. Marlino, L. E. O. Seiber, and H.-T. O. Lin, *Evaluation of the 2010 Toyota Prius Hybrid Synergy Drive System*, Mar 2011. [Online]. Available: <http://www.osti.gov/scitech/servlets/purl/1007833>
- [25] ANSYS, "Study of a permanent magnet motor with maxwell 2d : Example of the 2004 prius ipm motor," unpublished. [Online]. Available: <http://www.ansys.com>
- [26] R. Staunton, C. Ayers, J. U. T.-K. Chiasson, B. O. Burress, and L. Marlino, *Evaluation of 2004 Toyota Prius Hybrid Electric Drive System*, May 2006. [Online]. Available: <http://www.osti.gov/scitech/servlets/purl/890029>
- [27] J. Hsu, *Report on Toyota Prius Motor Thermal Management*, Feb 2005. [Online]. Available: <http://www.osti.gov/scitech/servlets/purl/885987>
- [28] J. Li, D.-W. Choi, D.-H. Son, and Y.-H. Cho, "Effects of mmf harmonics on rotor eddy-current losses for inner-rotor fractional slot axial flux permanent magnet synchronous machines," *Magnetics, IEEE Transactions on*, vol. 48, no. 2, pp. 839–842, Feb 2012.
- [29] (2014, Okt) Arnold Magnetic Technologies. Accessed 2014-10-13. [Online]. Available: http://www.arnoldmagnetics.com/Neodymium_Literature.aspx
- [30] (2014, Aug) Metalprices.com. Accessed 2014-08-05. [Online]. Available: <http://www.metalprices.com/dailysnapshots/Index>

- [31] (2014, Aug) Metal-pages.com. Accessed 2014-08-05. [Online]. Available: <http://www.metal-pages.com/>
- [32] (2011, Dec) Critical materials strategy. U.S. Department of energy. Accessed 2014-08-05. [Online]. Available: http://www.arnoldmagnetics.com/Rare_Earth_Information.aspx
- [33] (2012, jan) The important role of dysprosium in modern permanent magnets. Arnold Magnetic Technologies. Accessed 2014-08-05. [Online]. Available: http://www.arnoldmagnetics.com/Rare_Earth_Information.aspx
- [34] J. Hsu, *Report on Toyota/Prius Motor Design and Manufacturing Assessment*, Jul 2004. [Online]. Available: <http://www.osti.gov/scitech/servlets/purl/885676>
- [35] K. Kiyota, H. Sugimoto, and A. Chiba, "Comparing electric motors: An analysis using four standard driving schedules," *Industry Applications Magazine, IEEE*, vol. 20, no. 4, pp. 12–20, July 2014.